Three-dimensional Modeling of Cracking with Thermo-hydromechanical Process by Considering Rock Heterogeneity

Zhan Yu, Jianfu Shao, Yue Sun, Minh-Ngoc Vu, Carlos Plua, Gilles Armand

Three-dimensional Modeling of Cracking with Thermo-hydromechanical Process by Considering Rock Heterogeneity

Article *in* Rock Mechanics and Rock Engineering · September 2023

DOI: 10.1007/s00603-023-03536-4

CITATIONS
0

READS
212

6 authors, including:

Zhan Yu
Université de Lille
18 PUBLICATIONS **74** CITATIONS
SEE PROFILE

Sun Yue
Université de Lille
13 PUBLICATIONS **128** CITATIONS
SEE PROFILE

Ngoc Minh Vu
French National Radioactive Waste Management Agency (Andra)
211 PUBLICATIONS **1,651** CITATIONS
SEE PROFILE

Carlos Plua
Andra
30 PUBLICATIONS **223** CITATIONS
SEE PROFILE

Three-dimensional modeling of cracking with thermo-hydromechanical process by considering rock heterogeneity

Zhan YU[a,b], Jianfu SHAO[b,c,*], Yue SUN[b], Minh-ngoc VU[d], Carlos PLUA[d], Gilles ARMAND[d]

[a] *Key Laboratory of Ministry of Education on Safe Mining of Deep Metal Mines, College of Resources and Civil Engineering, Northeastern University, Shenyang, 110819, China*
[b] *University of Lille, CNRS, EC Lille, LaMcube, UMR9013, 59000 Lille, France*
[c] *Institut Universitaire de France (IUF), France*
[d] *Andra, Chatenay Malabry, France*

Abstract

This study is part of numerical simulations performed on an in-situ heating test conducted by the French National Radioactive Waste Management Agency (Andra) at the Meuse/Haute-Marne Underground Research Laboratory (URL) to study the thermo-hydromechanical behavior of the host Callovo-Oxfordian COx claystone in quasi real conditions, through the international research project DECOVALEX. We present a numerical study of damage and cracking process in saturated claystone subjected to thermo-hydromechanical coupling by considering material heterogeneity distribution. For this purpose, a macroscopic elastic model is first determined by using two steps of homogenization by taking into account the effects of porosity and mineral inclusions. This model is implemented into a finite element code devoted to solving thermo-hydromechanical coupling problems. The nucleation and propagation of cracks are described by using an extended phase-field method, considering the effects of temperature and fluid pressure on the evolution of phase-field. The proposed model is applied to the numerical analysis of cracking process due to excavation and heating around a group of boreholes (CRQ). The numerical results of the 3D simulation are compared with in-situ measurements of temperature and pore pressure distribution. The excavation damage zone and heating fracture is reproduced and analysed according to the structure of the heating position and the heterogeneity of the rock.

Keywords: Hydro-thermal cracking, material anisotropy, heterogeneous rocks, claystone,

phase-field method, radioactive waste

Highlights

- A phase-field model is developed with thermo-hydromechanical processes;
- Both tensile and shear cracks are taken into account;
- Crack nucleation is emphasized by spatial heterogeneity of material properties;
- Cracking processes due to thermal-hydraulic interaction are analyzed in three-dimensional conditions.

1. Introduction

Clayey rocks are considered in France as a potential geological barrier for underground disposal of radioactive waste. In this context, it is necessary to investigate thermo-hydromechanical (THM) properties of such rocks and other materials involved in the storage facilities. For this purpose, under the coordination of the French National Agency for radioactive waste management (Andra), a series of in-situ experiments have been and are being carried out at the Bure Underground Research Laboratory (MHM URL). Detailed presentations of some experiments can be found in [1, 2, 3]. The main objective of those experiments is to investigate thermo-hydromechanical responses of the host Callovo-Oxfordian (COx) claystone and other components during excavation, heating, and gas injection. The results obtained from these experiments are used for the validation of numerical models developed for the analysis and design of the future geological storage project known as Cigeo.

In order to foster international collaboration in research on the geological disposal of radioactive waste, an active and long-standing international project called DECOVALEX has been established. Various topics and benchmark modeling studies have been investigated and performed [4, 5, 6].

*Corresponding author: jian-fu.shao@polytech-lille.fr

In the phase of DECOVALEX-2023, the task A1 has been proposed to improve the numerical models' ability to predict the mechanisms and processes of fracture initiation and growth in clayey rocks due to heating induced fluid pressure variation. In the task, the step 1.2 is to reproduce the THM responses of an in-situ heating experiment performed by Andra at the MHM URL in June 2019, called "Representative THM Behavior of a high-level waste (HLW) Cell" (CRQ). This experiment involved two heating phases, lasting two and one months respectively, separated by a cooling phase. It is an accelerated heating scenario with the aim of replicating an effective stress evolution path which is expected to close to that in the area around a HLW cell in the Cigeo project in a short period of time. The rock is quickly heated until the pore fluid pressure reaches a critical value for the possible creation of fractures.

Therefore, for the feasibility study of geological disposal of nuclear waste, the nucleation and evolution of cracks is an essential issue. Such cracks can be initiated during gallery excavation, temperature increase due to waste heat production, and gas pressure rise. They are also expected to progressively close due to self-sealing and healing process. During the last decades, different types of numerical methods have been developed for modeling cracking process. Without giving an exhaustive review, we can mention for instance enriched finite element methods [7] and extended finite element methods (XFEM) [8, 9, 10]. In those methods, it is needed to define specific criteria to describe the onset and propagation of cracks. Other types of methods, including various discrete element methods, have also been developed and can be used for modeling cracking processes. However, the description of progressive transition from diffuse deformation to localized cracking is still a pending issue. The analysis of three-dimensional multiple cracks is also a hard task.

Based on the variational principle for fracture mechanics [11], the so-called phase-field method has been developed [12, 13]. By the approximation of sharp cracks by a regularized crack density function and the minimization of a total energy functional, the phase-field method is particularly efficient to deal with the progressive nucleation of localized cracks under complex three dimensional problems. It is applied to modeling dynamic brittle fracture [14], extended to multi-physics problems [15], and plastic materials [16, 17], etc..

In many previous studies, the accent was put on tensile cracks. For rocks subjected to compressive stresses as in most rock engineering problems, shear cracks represent an essential mechanism. Some extensions have been proposed [18, 19], generally using a specific decomposition of energy functional into a tensile part and a shear part. However, some critical issues should still be addressed. Under compressive stresses, complex mixed cracking modes can be observed [20, 21]. The propagation of frictional shear cracks is not only effected by deviatoric stress but also by confining pressure. Different types of extensions have been proposed considering frictional contact of cracks [22, 23, 24, 25]. Another interesting approach is to introduce two independent phase fields, respectively representing the tensile and shear cracks [26, 27].

In the present study, the concept of two phase fields developed in our previous work [26] is adopted for modeling tensile and shear cracks. It is further extended to three-dimensional coupled thermo-hydromechanical problems. In particular, the influence of fluid pressure due to heating process on the initiation and propagation of cracks is taken into account. Moreover, the effect of material heterogeneity due to spatial variability of mineralogical composition of clayey rocks is also investigated. The numerical results are compared with experimental data obtained from in-situ experiments.

2. Phase-field method for thermo-hydromechanical problems

In this work, a saturated porous medium is assumed to occupy the volume Ω with the external boundary $\partial\Omega$. Three physical fields are considered to describe the thermo-hydromechanical behavior of this material: i) In the mechanical field, it has the body force $\mathbf{f}_b$ in Ω, the surface force $\mathbf{t}_N$ on the part of external boundary $\partial\Omega_f$ and the prescribed displacement $\overline{\mathbf{u}}$ on the complementary part external boundary $\partial\Omega_u$; ii) In the pore fluid pressure field, it has the fluid flux $\overline{\omega}$ on the external boundary $\partial\Omega_\omega$ and to the prescribed fluid pressure $\overline{p}$ on the external boundary $\partial\Omega_p$; iii) In the temperature field, it has the heat flux $\overline{\mathbf{q}}$ on the external boundary $\partial\Omega_q$ and the prescribed temperature change $\overline{\theta}$ on the external boundary $\partial\Omega_\theta$. In additional, in this THM problem the process of onset and propagation of crack is taken into account by using phase-field method.

Since it has been seen many times in the literature, it is the author choice to keep the writing as light and simple as possible, emphasizing only the several strong assumptions made and their consequences, for the sake of the reading.

2.1. Variational framework

Based on the spirit of Griffith theory, [11] proposed a variation approach for quasi-static brittle fracture. The nucleation and propagation of quasi-static cracking process are considered as the minimisation of energy function that comprises stored energy and energy necessary for crack formation. This variational framework is suitable to extended to consider the crack process on the mentioned saturated porous material subjected to THM loads. In this way, the total energy functional is developed as:

$$E(\boldsymbol{\varepsilon}^e, m, \theta, \Gamma) = E_e(\boldsymbol{\varepsilon}^e, m, \theta, \Gamma) + E_c(\Gamma) \tag{1}$$

where $E_c(\Gamma)$ is the fracture surface energy and $E_e(\boldsymbol{\varepsilon}^e, m, \theta, \Gamma)$ denotes the elastic strain energy of cracked material, which is a function of elastic strain tensor $\boldsymbol{\varepsilon}^e$, fluid mass change per unit initial volume m and variation of temperature θ, as well as the set of crack Γ.

2.1.1. Phase field model

Following the regularization strategy proposed by [12], the crack can be represented by the scalar phase field variable d, which has the range from 0 (intact material) to 1 (fully broken). Furthermore, in order to easily deal with mixed-mode cracks of rock-like material, a so-called double phase field method [28] is considered to introduce tensile damage d^t and shear damage d^s. In this way, the approximated crack surface area can be represented as:

$$A_\Gamma \approx A^t_\Gamma(d^t) + A^s_\Gamma(d^s) = \int_\Omega \{\gamma^t(d^t, \nabla d^t) + \gamma^s(d^s, \nabla d^s)\} d\Omega \tag{2}$$

where total surface area of sharp crack A_Γ is approximated by the volumetric integration of a crack density function for tensile crack $\gamma^t(d^t, \nabla d^t)$ and shear crack $\gamma^s(d^s, \nabla d^s)$. Among three commonly employed phase-field models proposed by [12, 29, 30], we adopt the formulation presented by [29], which can be expressed as follows:

$$\gamma^\alpha(d^\alpha, \nabla d^\alpha) = \frac{1}{2}\{\frac{1}{l_d}(d^\alpha)^2 + l_d \nabla d^\alpha . \nabla d^\alpha\} \quad ; \quad \alpha = t, s \tag{3}$$

where l_d denotes a length scale parameter which is in relation with the width of smeared cracks. The crack density functions, denoted as $\gamma^\alpha(d^\alpha, \nabla d^\alpha)$, are dependent on both the damage variables d^α and their gradients ∇d^α. This non-local formulation enables the regularization of damage localization issues. With the help of the approximation work, Equation (1) can be rewritten as:

$$E(\boldsymbol{\varepsilon}^e, m, \theta, d^t, d^s) = \int_\Omega w_e(\boldsymbol{\varepsilon}^e, m, \theta, d^t, d^s)d\Omega + \int_\Omega w_c(d^t, d^s, \nabla d^t, \nabla d^s)d\Omega \tag{4}$$

with elastic strain energy of cracked material w_e, and the energy density per unit volume requested to create the crack w_c:

$$w_c(d^t, d^s, \nabla d^t, \nabla d^s) = g_c^t \gamma^t(d^t, \nabla d^t) + g_c^s \gamma^s(d^s, \nabla d^s) \tag{5}$$

2.1.2. Elastic free energy

For an intact saturated porous medium, the constitutive relations due to thermo-poroelastic theory [31, 32] can be expressed as:

$$\boldsymbol{\sigma} - \boldsymbol{\sigma}^0 = \mathbb{C}_b^0 : \boldsymbol{\varepsilon}^e - b\boldsymbol{I}(p - p^0) - 3K_b\alpha_b\boldsymbol{I}\theta \tag{6}$$

$$p - p_0 = M(-b\boldsymbol{I} : \boldsymbol{\varepsilon}^e + \frac{m}{\rho_f^0}) + 3\alpha_m M\theta \tag{7}$$

$$s - s_0 = s_m^0 m + \alpha_b \boldsymbol{I} : (\boldsymbol{\sigma} - \boldsymbol{\sigma}^0) - (3\alpha_m - b\alpha_b\boldsymbol{I})(p - p_0) + \frac{C_\sigma^b}{T_0}\theta \tag{8}$$

For the sake of readability, the mentioned symbols are explained in nomenclature. In this study, though the initial anisotropy of elastic properties of COx claystone is taken into account, for the sake of simplicity, the tensors of Biot coefficients, thermal dilation coefficients and drained thermo-elastic coupling coefficients are taken as isotropic ones. In order to deal with anisotropic elastic materials, the so-called Reuss equivalent bulk modulus is here used: $K_b = k_{Reuss}(d^t, d^s)$. The Biot modulus is accordingly given by $1/M = (b - \phi)/K_m + \phi/K_f$. The differential thermal coefficient is given by $\alpha_m = (b - \phi)\alpha_b + \phi\alpha_f$. By using these constitutive relations, the elastic free energy of an intact material can be determined as:

$$w_e^0(\boldsymbol{\varepsilon}^e, p, \theta) = \frac{1}{2}\boldsymbol{\sigma}_b : \boldsymbol{\varepsilon}^e + \frac{1}{2}\frac{(p - p_0)^2}{M} - \frac{1}{2}\frac{C_\sigma^b}{T_0}\theta^2 \tag{9}$$

with Biot effective stress tensor σ_b:

$$\boldsymbol{\sigma}^b = (\boldsymbol{\sigma} - \boldsymbol{\sigma}^0) + \boldsymbol{B}(p - p_0) \tag{10}$$

Given that the effective stress plays an important role in the onset and propagation of cracking process for saturated rock-like material, we decompose the Biot effective stress into a tensile part and a compressive part:

$$\begin{cases} \boldsymbol{\sigma}^{b+} = \mathbb{P}_\sigma^+ : \boldsymbol{\sigma}^b \\ \boldsymbol{\sigma}^{b-} = \mathbb{P}_\sigma^- : \boldsymbol{\sigma}^b \end{cases} \tag{11}$$

with the operators for spectral decomposition of stress tensor $\mathbb{P}_\sigma^\pm$ proposed in [33, 34]. Assuming the extension behavior is affected by tensile crack and the compression behavior is mainly influenced by shear crack, the elastic free energy of the damaged material can be expressed as:

$$w_e(\boldsymbol{\varepsilon}^e, p, \theta, d^t, d^s) = h_t(d^t) w_e^{0+} + h_s(d^s) w_e^{0-} + \frac{1}{2}\frac{(p - p_0)^2}{M} - \frac{1}{2}\frac{C_\sigma^b}{T_0}\theta^2 \tag{12}$$

with

$$\begin{cases} w_e^{0+} = \frac{1}{2}\boldsymbol{\sigma}^{b+} : \boldsymbol{\varepsilon}^e \\ w_e^{0-} = \frac{1}{2}\boldsymbol{\sigma}^{b-} : \boldsymbol{\varepsilon}^e \end{cases} \tag{13}$$

The decomposition of Biot effective stress tensor is due to the operators $\mathbb{P}_\sigma^\pm$ (see the detail of old study [35]). A common form $h_\alpha(d^\alpha) = (1-k)(1-d^\alpha)^2 + k$ with $\alpha = t, s$ is used to represent the degradation of failure process. In this study, $k = 1 \times 10^{-9}$ is applied to avoid the calculating error after the material is fully broken ($d^\alpha = 1$).

2.1.3. Evolution of crack fields

Given that all the terms of total energy functional are obtained and introduced, the governing equations for tensile crack d^t and shear crack d^s can be determined by solving the

minimization problem of Equation (4):

$$\begin{cases} -\dfrac{\partial w_e}{\partial d^\alpha} - g_c^\alpha \delta_{d^\alpha} \gamma^\alpha = 0 \quad , \quad \dot{d^\alpha} > 0 \quad , \quad \text{in} \quad \Omega \\ \\ -\dfrac{\partial w_e}{\partial d^\alpha} - g_c^\alpha \delta_{d^\alpha} \gamma^\alpha \leq 0 \quad , \quad \dot{d^\alpha} = 0 \quad , \quad \text{in} \quad \Omega \\ \\ \dfrac{\partial \gamma}{\partial \boldsymbol{\nabla} d^\alpha}.\mathbf{n} = 0 \quad , \quad \text{on} \quad \delta\Omega \end{cases} \tag{14}$$

More precisely, the evolution of two crack fields are described by the following equations:

$$\begin{cases} -h_t'(d^t) w_{e+}^0 - g_c^t \left\{ \frac{1}{l_d} d^t - l_d \Delta d^t \right\} = 0 \quad , \quad \dot{d^t} > 0 \\ \\ -h_s'(d^s) w_{e-}^0 - g_c^s \left\{ \frac{1}{l_d} d^s - l_d \Delta d^s \right\} = 0 \quad , \quad \dot{d^s} > 0 \end{cases} \tag{15}$$

where the two elastic energy of intact material w_e^{0+} and w_e^{0-} are represented in Equation (13). It is reasonable to define the tensile crack evolution is driven by the positive part of elastic energy w_e^{0+}. On the other hand, given that the pure compression behavior can not contribute to create the shear crack, only a part of negative part of elastic energy w_e^{0-} can be seen as the driving quantity for compressive-shear crack (see [28] for detail):

$$w_-^s = \frac{1}{2G} \langle \frac{\langle \sigma_1^t \rangle_- - \langle \sigma_3^t \rangle_-}{2cos\varphi} + \frac{\langle \sigma_1^t \rangle_- + \langle \sigma_3^t \rangle_-}{2} tan\varphi - c \rangle_+^2 \tag{16}$$

with the bracket $\langle . \rangle_\pm$ such as:

$$\begin{cases} \langle a \rangle_+ = a, \quad \langle a \rangle_- = 0, \quad a \geq 0 \\ \langle a \rangle_+ = 0, \quad \langle a \rangle_- = a, \quad a < 0 \end{cases} \tag{17}$$

with cohesion c and friction angle φ of material. The major and minor Terzaghi effective principal stress σ_1^t and σ_3^t are considered according to the study [36, 37]. By substituting the physically-based driving energy into (15), w_{e-}^0 can be replaced by w_-^s. Finally, based on the concept of [13], two energy history functionals are defined as follows:

$$\begin{cases} \mathcal{H}^t(t) = max[w_{e+}^0(\tau)]_{\tau \in [0,t]} \\ \mathcal{H}_-^s(t) = max[w_-^s(\tau)]_{\tau \in [0,t]} \end{cases} \tag{18}$$

Given that the history functionals H^t and H^s_- are used instead of w^0_{e+} and w^s_- in the evolution equation of tensile and shear crack respectively, the irreversibility of cracking process is taken into account.

3. Numerical implementation in finite element method

The THM problem considering tensile and shear crack can be solved by using the framework of finite element method. According to Equations (6), (7), (8) and (15), the weak forms for five unknown fields are expressed as:

$$\int_\Omega \delta\boldsymbol{\varepsilon} : \mathbb{C}^b(d^t, d^s) : \boldsymbol{\varepsilon} dV - \int_\Omega \delta\boldsymbol{\varepsilon} : (\delta p)\boldsymbol{I} dV - \int_\Omega \delta\boldsymbol{\varepsilon} : (3\alpha_b K_b(d^t, d^s)T)\boldsymbol{I} dV = \int_{\Omega_f} \boldsymbol{t}.\delta\boldsymbol{u} dS \quad (19)$$

$$\begin{aligned}\int_\Omega \frac{\boldsymbol{k}(d^t)}{\mu}\nabla p.\nabla(\delta p)dV = &\int_{\Omega_\omega} \frac{\boldsymbol{k}(d^t)}{\mu}\delta p.\nabla p\bar{n}dS - \int_\Omega \frac{1}{M}\frac{\partial p}{\partial t}\delta p dV \\ &- \int_\Omega b\frac{\partial \varepsilon_{kk}}{\partial t}\delta p dV + \int_\Omega 3\alpha_m \frac{\partial \theta}{\partial t}\delta p dV\end{aligned} \quad (20)$$

$$\begin{aligned}\int_\Omega \lambda\nabla T.\nabla(\delta\theta)dV = &\int_{\Omega_q} \lambda\delta T\nabla T.\bar{n}dS - \int_\Omega C^b_\varepsilon \frac{\partial\theta}{\partial t}\delta\theta dV - \int_\Omega (3\alpha_b K_b(d^t, d^s)T_0)\frac{\partial\varepsilon_{kk}}{\partial t}\delta\theta dV \\ &+ \int_\Omega (3\alpha_m T_0)\frac{\partial p}{\partial t}\delta\theta dV + \int_\Omega \frac{\boldsymbol{k}(d^t)}{\mu}\nabla p.(C_p\nabla\theta)\delta\theta dV\end{aligned} \quad (21)$$

$$\int_\Omega \{(g^t_c/l_d + 2\mathcal{H}_t)d^t\delta d^t + g^t_c\nabla d^t\cdot\nabla(\partial d^t)\}dV = \int_\Omega 2\mathcal{H}_t\partial d^t dV \quad (22)$$

$$\int_\Omega \{(g^s_c/l_d + 2\mathcal{H}^s_-)d^s\delta d^s + g^s_c\nabla d^s\cdot\nabla(\partial d^s)\}dV = \int_\Omega 2\mathcal{H}^s_-\partial d^s dV \quad (23)$$

Among these relations, the effect of damage is mainly realized on mechanical field and pore pressure field according to the elastic stiffness of undamaged material:

$$\mathbb{C}_b(d^t, d^s) = \left\{h_t(d^t)\mathbb{P}^+_\sigma + h_s(d^s)\mathbb{P}^-_\sigma\right\} : \mathbb{C}^0_b \quad (24)$$

and the permeability tensor of cracked porous medium:

$$\boldsymbol{k}(d^t, d^s) = \boldsymbol{k}_0\exp(\eta_k\max(d^t, d^s)) \quad (25)$$

with the elastic stiffness of undamaged material $\mathbb{C}_b^0$, evolution rate of permeability η_k and the initial permeability tensor of intact porous medium $\boldsymbol{k}_0$. The drained bulk modulus $K_b(d^t, d^s)$ can be calculated according to obtained $\mathbb{C}_b(d^t, d^s)$. The damage effect for thermal parameters of the material is ignored in this study.

In the framework of the finite element method, following the previous work, the THM coupling problem formulation [26] and the formulation of the tensile and shear crack problem [28] can be solved. Considering the physical characteristic of the rock material, the temperature field is solved by an explicit decoupled algorithm, as it is not sensitive to the effects of the mechanical field, the pore pressure field and the damage fields. In order to save the computation memory and time, the fixed stress iteration [38] is used to solve the hydromechanical coupling. And the so-called Alternate Minimization (AM) solver proposed in [12, 39] is used to couple the displacement field and phase fields because of its good robustness performance.

4. Consideration of material heterogeneity

In rock-like materials, cracks often start due to variations in the material, such as at interfaces between stiff inclusions and a weak matrix, or in weak zones with high porosity. Previous studies have used a numerical trick of placing weak elements in the material to facilitate crack initiation and propagation. However, in this work, we use a micro-mechanics based approach to more accurately reflect the effect of material heterogeneity on mechanical properties. Specifically, we use an analytical homogenization method to determine macroscopic elastic properties as explicit functions of porosity and inclusion volume fraction at the microscopic scale.

For this study, we focus on the Callovo-Oxfordian (COx) claystone, which has been widely studied in France for its potential use in storing radioactive waste. Previous research [40] has identified two main scales of interest for this material: at the mesoscopic scale, mineral particles like quartz, calcite, and pyrite are randomly distributed in a clay matrix; at the microscopic scale, the majority of pores are found inside the clay matrix.

In order to determine the macroscopic elastic properties, two steps of linear homogenization is performed considering two micro-structure parameters: the porosity of the clay matrix f_p and the volume fraction of mineral inclusions f_i, one gets:

$$f_p = \frac{\Omega_p}{\Omega_p + \Omega_m} \tag{26}$$

$$f_i = \frac{\Omega_i}{\Omega_i + \Omega_p + \Omega_m} \tag{27}$$

Ω is the volume of representative volume element, while Ω_p, Ω_i and Ω_m are respectively the volumes occupied by pores, inclusions and solid clay matrix. To account for the inclusion-matrix morphology, we use the standard Mori-Tanaka scheme for each homogenization step [41]. In the first step, we determine the effective elastic tensor of the porous matrix ($\mathbb{C}^{mp}$) by considering the effect of porosity. One gets:

$$\mathbb{C}^{mp} = (1 - f_p)\mathbb{C}^m : [(1 - f_p)\mathbb{I} + f_p(\mathbb{I} - \mathbb{P}^p : \mathbb{C}^m)^{-1}]^{-1} \tag{28}$$

$\mathbb{P}^p(\mathbb{C}^m)$ is the fourth order Hill tensor for ellipsoidal pores [42, 43], $\mathbb{C}^m$ is the elastic tensor of solid matrix, and $\mathbb{I}$ is the fourth order unit tensor. At the mesoscopic step of homogenization, the macroscopic elastic tensor of heterogeneous rocks is determined after including the influence of mineral inclusions:

$$\mathbb{C}^{hom} = \mathbb{C}^{mp} + [f_i(\mathbb{C}^{in} - \mathbb{C}^{mp}) : \mathbb{D}^{in}] : [\mathbb{I} + f_i(\mathbb{C}^{in} - \mathbb{I})]^{-1} \tag{29}$$

with

$$\mathbb{D}^{in} = [\mathbb{I} + \mathbb{P}^i : (\mathbb{C}^{in} - \mathbb{C}^{mp})]^{-1} \tag{30}$$

$\mathbb{P}^i(\mathbb{C}^{mp})$ is the Hill tensor for spherical inclusions [42, 43]. It is worth noting that, we combine different families of mineral particles into a single equivalent inclusion phase, and represent its elastic stiffness tensor as $\mathbb{C}^{in}$.

Since the spatial variability of macroscopic elastic properties in COx claystone is attributed to the non-uniform distribution of porosity and inclusion concentration, in this study, we assume a random distribution of porosity (f_p) and volumetric fraction of mineral inclusions (f_i) using the standard Weibull distribution function:

$$\xi_\alpha = \frac{m_\alpha}{\beta_\alpha}(\frac{f_\alpha}{\beta_\alpha})^{m_\alpha - 1} exp[-(\frac{f_\alpha}{\beta_\alpha})^{m_\alpha}] \quad , \alpha = p, i \tag{31}$$

where f_α is the volume fraction of pores ($\alpha = p$) and mineral inclusions ($\alpha = i$). β_α is the scale parameter of the distribution which represents the mean value of random variable. m_α is the homogeneity index of the material.

In this study, we have adopted an elastic-damage model. Plastic deformation is neglected. Moreover, there exist theoretical homogenization models for predicting macroscopic elastic properties with mineral compositions and porosity. Therefore, it seems to be a good choice to consider effect of material heterogeneity on elastic properties.

5. Numerical simulation

In this section, the proposed THM modeling, which takes into account the double phase field method, is applied to simulate the results of the in-situ CRQ test performed at Andra's Underground Research Laboratory (URL) [44]. The simulation focuses on capturing the thermo-hydromechanical responses and failure behavior of COx claystone during excavation and heating-cooling processes.

5.1. General presentation of CRQ test

Figure 1 provides a partial view of the Andra URL, which is situated at a depth of -490 m. The study focuses on the GCS gallery located within the COx claystone layer. The CRQ (Representative THM Behavior of a HLW Cell) in-situ experiment was performed in the GCS gallery, as shown in Figure 1 (right). The experiment involved drilling ten 20 m long heater boreholes (CRQ1701-CRQ1710) horizontally from the GCS drift wall, with the heaters installed in the last 10 m. In addition, sixteen sensors were positioned in four additional boreholes (CRQ1720-CRQ1723) to monitor temperature and pore pressure. The aim of the experiment was to examine the cracking process resulting from the THM behavior of the rock, with the anticipated fracture location being between the two central boreholes and 15 m from the GCS drift wall, which is at the mid-plane of the heater devices.

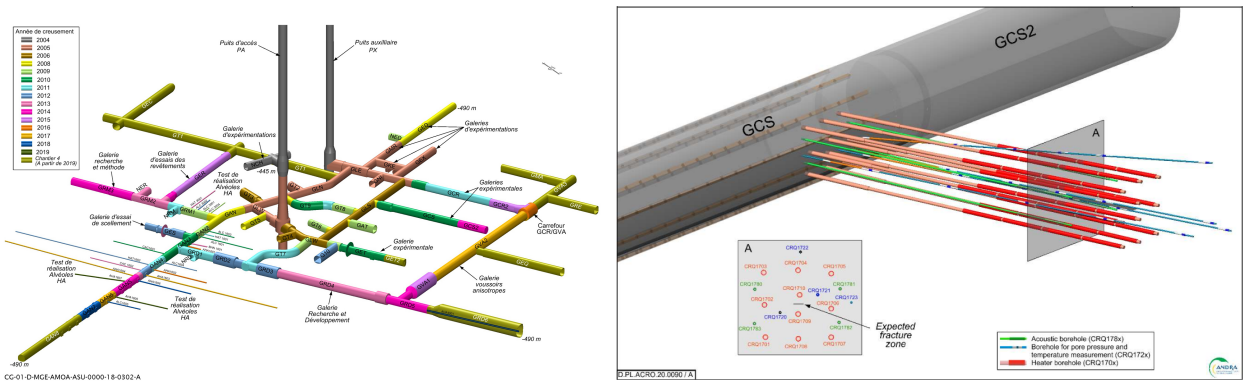

Figure 1: Partial view of Andra URL [44] (left) and view of CRQ heating test (right)

Two heating phases were performed using the mentioned heaters, and the heat power applied is shown in Figure 2. It is worth noting that the heater devised in CRQ1704 was damaged after the first heating phase. Therefore, the second heating phase was only heated by the remaining nine heater devices.

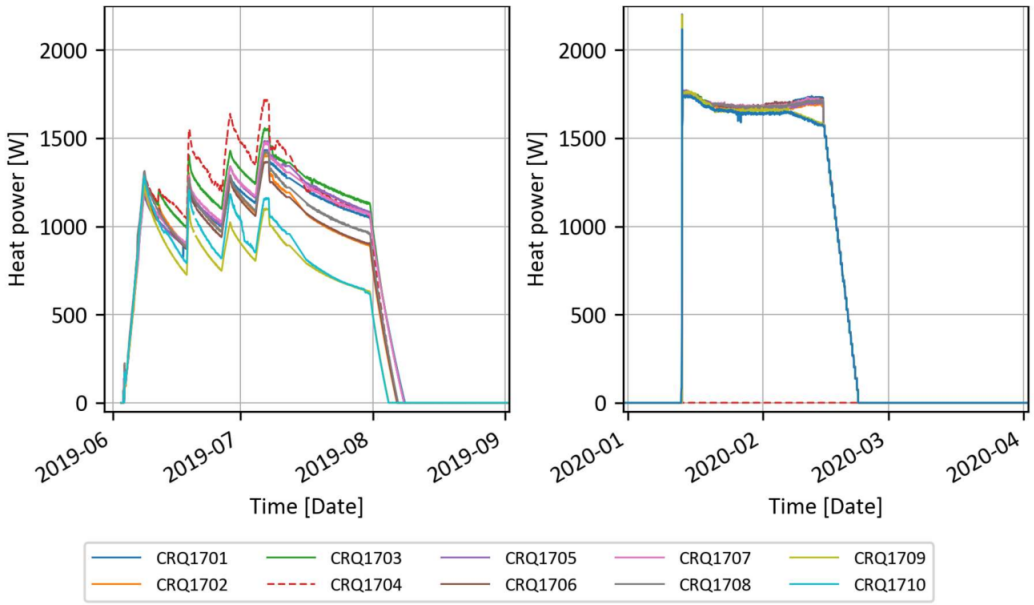

Figure 2: Timeline of the CRQ experiment with evolution of the heat power history of each heater device: (Left) first heating phase and (Right) second heating phase (provided by task specification)

5.2. Input data of modeling

As shown in Figure 3 (left), the studied 3D domain consists of a cube with dimensions of 50 m × 50 m × 50 m in order to represent the far field. On one surface of the studied cube, half of the GCS drift with 5.2 m diameter is located. Ten heater boreholes with a diameter of 0.172 m and a length of 20 m are placed on the wall of the GCS drift. The detailed coordinates of these ten heater boreholes are shown in the appendix. For simplicity, the four boreholes with sensors are not included. In this way, 883,232 tetrahedral elements with 148,807 nodes are used to mesh the studied domain, as shown in Figure 3 (right). Since the rock around the heaters is expected to be damaged, the finest mesh is defined for this heater part, which is 10-20 m deep from the GCS drift wall. This is balanced choice between a fine description of damaged zones and computation costs such as computing memory and time used.

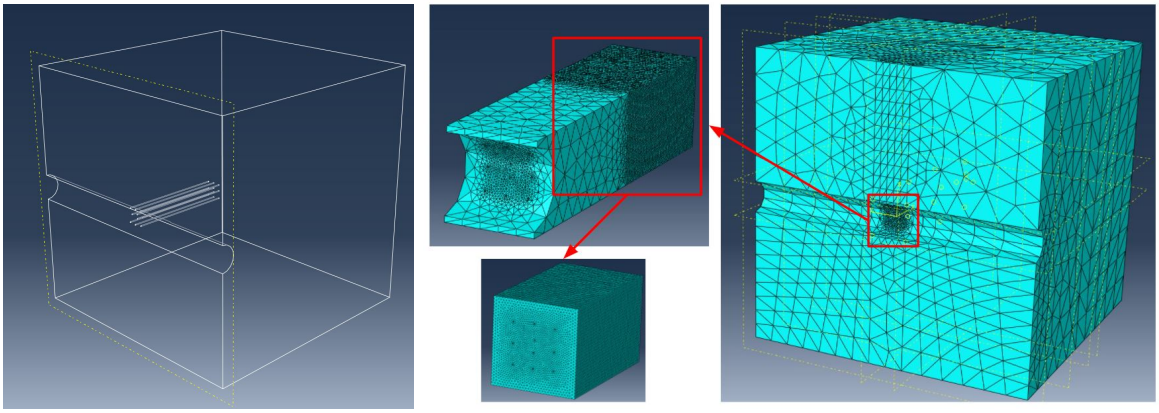

Figure 3: Geometry and mesh of CRQ simulation

Based on the study of [1, 45], the initial stress state of the studied domain is defined as follows: i) the minimum principal stress σ_h is -12.4 MPa (parallel to the heater boreholes); ii) the maximum principal stress σ_H is -16.1 MPa (parallel to the GCS gallery); and iii) the vertical principal stress σ_v is -12.7 MPa (perpendicular to the heater boreholes and GCS gallery). The initial temperature and pore pressure of the whole domain are assumed to be uniform, with T_0 = 22°C and p_0=4.7 MPa, which are the values at a depth of -490 m from the ground.

The boundary conditions are defined as shown in Table 1. The lateral faces are considered to have symmetrical conditions for all THM fields. The top and bottom faces are permeable to heat flux and fluid flux. After excavation of the GCS gallery, the drift wall is not fixed for displacement but is fixed for pore pressure at 0.1 MPa. The temperature of the gallery is applied based on the values measured during the experiment. The boundary conditions for the boreholes is changed while the heating phase begins. The surface of the drift changes from permeable to impermeable due to the installation of the resin.

Table 1: Boundary conditions of the CRQ simulation

Boundary	Thermal	Hydraulic	Mechanical
Lateral faces	Free surface	Free surface	Zero normal displacement
Top face	$22°C$	4.7 MPa	-12.7 MPa
Bottom face	$22°C$	4.7 MPa	Zero normal displacement
GCS drift wall	T(t)	0.1 MPa	Free surface
Borehole wall (before heating)	Free surface	0.1 MPa	Free surface
Borehole wall (during heating)	Free surface	Free surface	Free surface

According to previous studies [46], the COx claystone is considered to be a transversely isotropic material with regards to elastic modulus, failure strength, thermal, and hydraulic properties. For simplicity, only the initial anisotropy of elastic properties, permeability, and thermal conductivity is considered, while the other parameters are assumed to be isotropic. Following the previous experiment [47] and simulation work [48] for a laboratory-scale heating test on the same rock, material parameters are provided as shown in Table 2. It is important to highlight that the measured parameters in the experiment can be influenced by several factors, including potential variable discrepancies and inherent variability among individual rock samples. The material parameters employed in this simulation have been carefully calibrated, taking into account the distinctions between laboratory-scale and in-situ tests. This calibration falls within an appropriate range, informed by the accumulated knowledge of COx claystone from ANDRA's experience.

The regular parameters of water are used in this work. For simplicity, the following parameters are considered as constant: bulk modulus of water $K_f = 2.2$ GPa, density of water $\rho_f = 1000$ kg/m^3, heat capacity of water $C_f = 4180$ J/kg/K. The water dynamic viscosity μ_f (Pa·s) is due to temperature ($^\circ C$), it has:

$$\mu_f(T) = 4.2844 \times 10^{-5} + (0.157(T + 64.993)^2 - 91.296)^{-1} \tag{32}$$

And the volumetric thermal expansion of water ($1/^\circ C$) is also dependent on temperature ($^\circ C$):

$$\alpha_f(T) = -6T^4 + 1660T^3 - 197796T^2 + 16862446T - 64319951 \tag{33}$$

It is worth noting that, for the reason of comparison between different teams which worked on this simulation of in-situ test, Andra proposed that these two parameters are the most sensitive ones to temperature variation.

Furthermore, since the phase field method is applied to describe the cracking process in this study, the parameters defined in this numerical method should be chosen carefully as shown in Table 3. Although scale length l_d is a defined parameter which controls the width of localized damage, it also serves as a material property within phase-field modeling. This is due to the fact that the peak stress of a material is determined by the scale length in conjunction with the toughness parameter and elasticity parameters [16, 49]. For the evolution of tensile damage, one gets:

$$\sigma_t = \sqrt{g_c^t \frac{E_{eq}}{3l_d}} \tag{34}$$

with the average value of uniaxial tensile strength for COx claystone $\sigma_t = 3$ MPa, and the equivalent isotropic elastic modulus $E_{eq} = (E_\parallel \times E_\parallel \times E_\perp)^{1/3}$. Following the work of [13], a scale length is defined according to the element size h used in the area predicted to formation of damage: $l_d = 2h$. On the other hand, according to Equation (15), the evolution of shear damage zone is due to three parameters: toughness coefficient of shear damage g_c^s, friction angle φ and cohesion c. It is noticed that although the physical significance of the friction and cohesion is the same as that widely adopted, their values in the context of phase-field model are generally different with those used in classical Mohr-Coulomb criterion. Their value are

chosen so that one obtains reasonable values of uniaxial compression strength and tensile strength. The detailed explanation of the choice of these parameters for COx claystone is presented in the previous study [35]. Moreover, the scale length l_d, which controls the width of localized damage, is determined by the element size. In this study, the value used is twice the element size of the predicted damaged area. The permeability variation coefficient η_k, defined in Equation (25), is identified with the help of experimental work [50], and it has worked well in previous numerical studies [35] that considered 2D problems for the same rock.

Only the excavation damage zone (EDZ) around the GCS drift is considered. The EDZ is located in the area with a depth of 2.6 m from the GCS drift wall. The permeability is increased by 10 times the initial value in this zone. In this way, after the excavation of the GCS gallery, there is a gradient of pore pressure close to the drift wall due to the seepage phenomenon. Comparing the pore pressure measured by the sensor around the GCS gallery on 2018/7/31, as shown in Figure 4, the numerical results show good agreement with the effect of the EDZ. It is indeed worth noting that the main feature of the pore pressure distribution that needs to be reproduced is influenced by the EDZ of the GCS gallery. However, it's important to acknowledge that the modeling of GCS excavation in this study has certain limitations. For example, the mesh around the GCS may not be fine enough, and the time-dependent behavior during the excavation process is not taken into account.

Table 2: Material parameters for COx claystone from [47]

Parameters	Unit	Notation	Value
Young's modulus (parallel to bedding)	10^9 Pa	$E_{\parallel}$	6.0
Young's modulus (perpendicular to bedding)	10^9 Pa	$E_{\perp}$	4.0
Poisson ratio (Parallel to bedding)	-	$\mu_{\parallel\parallel}$	0.3
Poisson ratio (Perpendicular to bedding)	-	$\mu_{\perp\parallel}$	0.3
Shear modulus (Perpendicular to bedding)	10^9 Pa	$G_{\perp\parallel}$	1.7
Density of solid grains	kg/m^3	ρ_s	2770
Biot coefficient	-	b	0.8
Porosity	-	ϕ	0.18
Initial permeability (parallel to bedding)	10^{-20} m^2	$k^0_{\parallel}$	4.0
Initial permeability (perpendicular to bedding)	10^{-20} m^2	$k^0_{\perp}$	1.33
Equivalent thermal conductivity (parallel to bedding)	W/m/K	$\lambda_{\parallel}$	2.1
Equivalent thermal conductivity (perpendicular to bedding)	W/m/K	$\lambda_{\perp}$	1.28
Heat capacity of porous medium	J/kg/K	C_p	1050
Volumetric thermal expansion of solid grains	10^{-5} 1/K	α_s	4.5

Table 3: Parameter of phase field model for CRQ simulation

Parameters	Value
Material toughness	g_c^t=4500 N/m; g_c^s=500 N/m
Friction angle	φ=15°
Cohesion	c=0.1 MPa
Scale length	l_d=0.18 m
Permeability variation	η_k=40

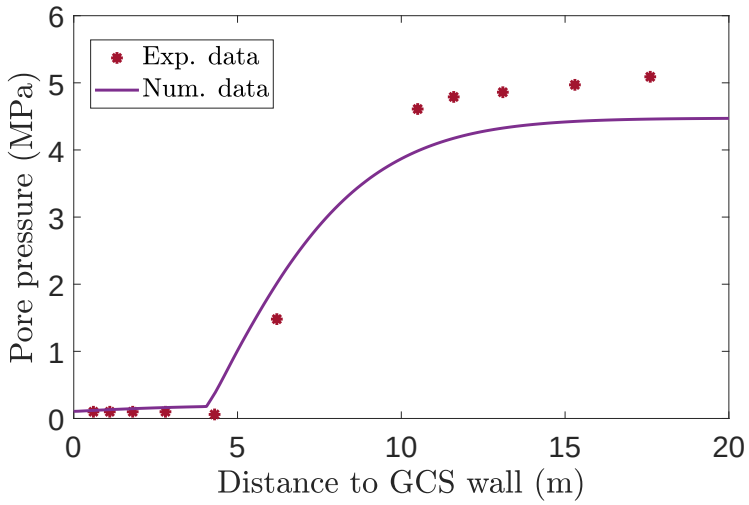

Figure 4: Pore pressure evolution around the GCS drift at 2018/7/31, comparing the experimental result and numerical result

The simulation is applied from the excavation of the GCS gallery to the end of the second cooling phase. The detailed dates of the main operations are shown in the appendix. For better readability, in the following numerical presentations, the dates are replaced by days, where day t=0 is defined as the day before the excavation of the GCS gallery.

5.3. Simulation results

Figure 5 shows the variation of temperature over time at the sixteen sensor points located in four boreholes: CRQ1720-1723. The two peaks in the figure correspond to the end of the first heating phase and the second heating phase. By comparing the experimental and numerical results, it is clear that the tendencies are well-reproduced and the peak values are almost identical. The peak values of the second heating are higher than the peak values of the first heating, except for the points on CRQ1722. This is because the heater CRQ1704 was damaged during the second heating phase, and CRQ1722 is the closest borehole to the damaged heater. Nevertheless, it should be noted that reproducing the temperature evolution in the in-situ test scale is relatively straightforward due to the fact that the heat transfer process in the rock-like material remains unaffected by initial fracture or crack nucleation.

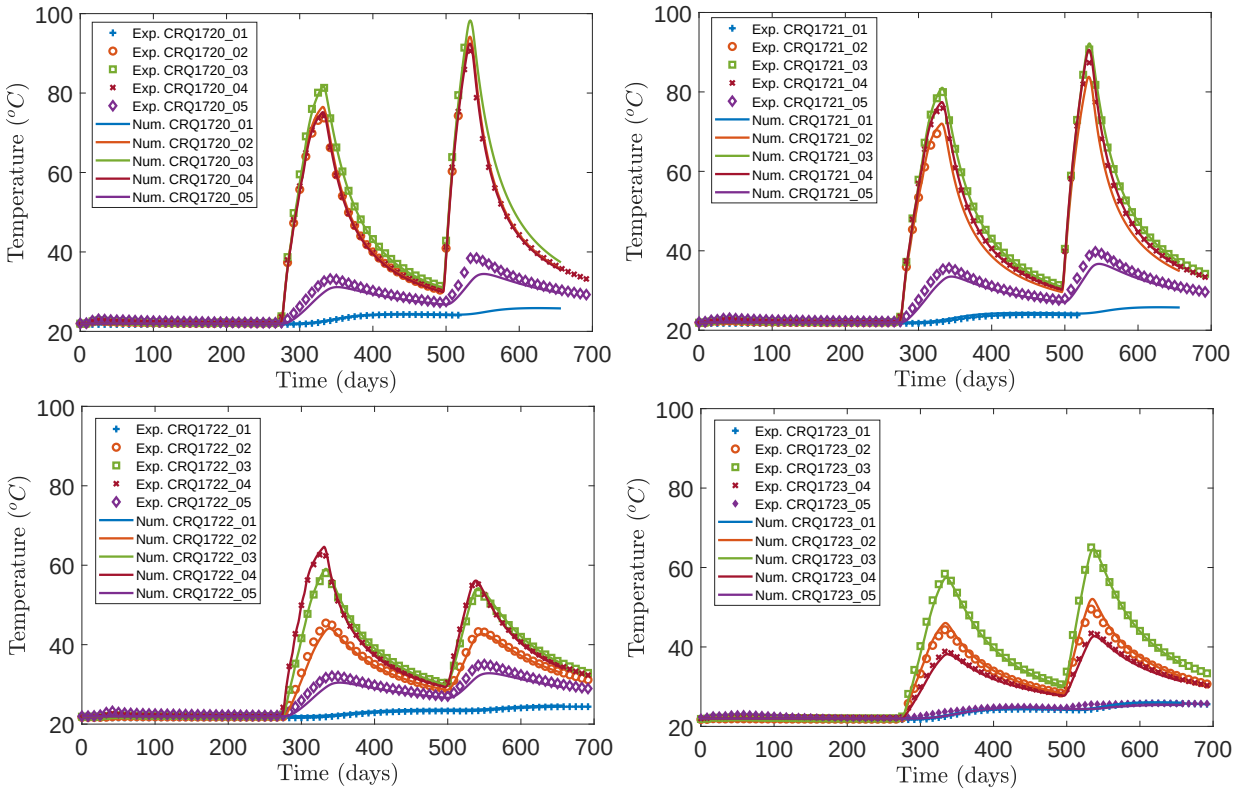

Figure 5: Evolution of temperature at the sensor points of CRQ 1720-1723, comparing the experimental results and numerical results

Figure 6 illustrates the temperature distributions at the end of the first heating phase and the end of the second heating phase. The temperature concentration area plays an important role to study the thermal damage. The middle plane of the heating section is expected to exhibit the highest temperatures. Hence, this plane is selected to analyze the THM coupling behavior resulting from heating. After the completion of the first heating phase, it is evident that the region with the highest temperature is concentrated around the two middle boreholes, namely CRQ1709 and CRQ1710. However, at the end of the second heating phase, a shift in the position of the zone with the highest temperature can be observed. This change is attributed to the damage sustained by the heater in CRQ1704 (the top center borehole), causing the zone of elevated temperature to relocate towards the lower of the two central boreholes, as depicted in the isothermal map.

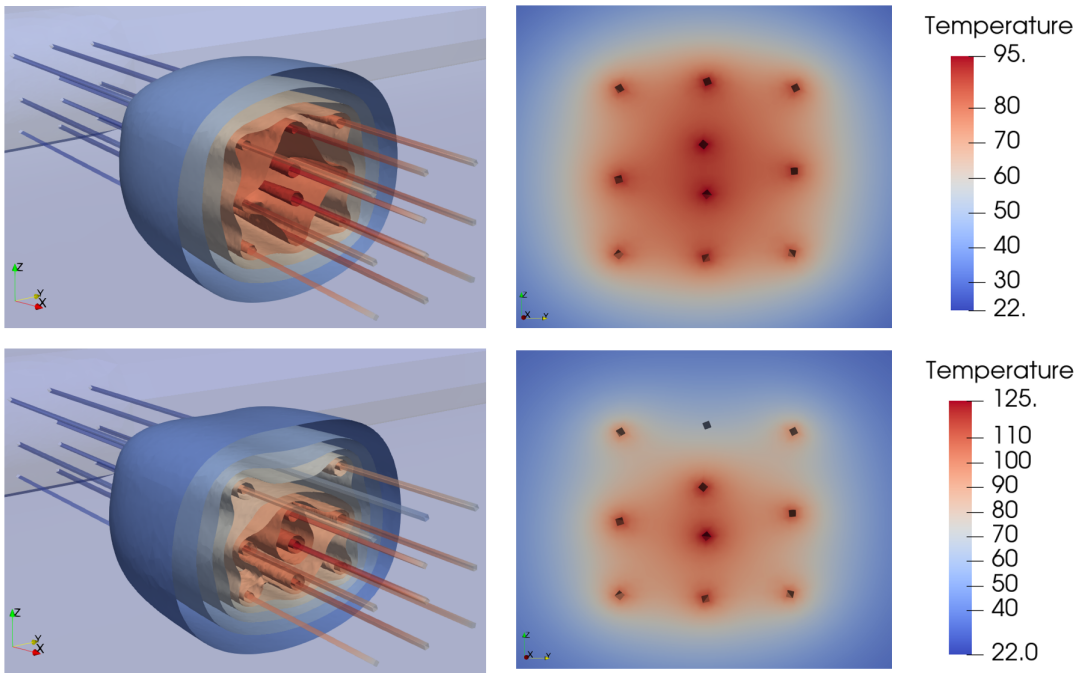

Figure 6: Distribution of temperature ($°C$) at the end of the first heating phase (top) and the end of second heating phase (bottom)

The onset of damage is mainly caused by the operation of excavation and heating during the CRQ test. As shown in Figure 7, the damage due to the excavation of boreholes is reproduced as the shear damage. This damage creates what is known as a borehole damaged zone (BDZ), a phenomenon commonly observed in in-situ experiments with COx claystone. The maximum value of the shear damage variable d^s is about 0.23, which indicates that only micro-cracking occurs around the boreholes, and not macro-cracking. These micro-cracks lead to increased permeability, which is a consequence of pores being connected by fractures, as described in Equation (25).

We visualize in Figure 8 the region with higher permeability due to the excavation, with elements having permeability values 10 times higher than the initial permeability being highlighted. It can be seen that these elements within the BDZ eventually form a tube that connects with the excavation damaged zone (EDZ) of the GCS gallery. As mentioned previously, the borehole walls are defined as impermeable due to the installation of the resin. As a result, water can easily flow to the GCS gallery through the connected high-permeability

zones. This phenomenon is verified in the in-situ test according to the observation of the seepage around the boreholes on the GCS drift wall.

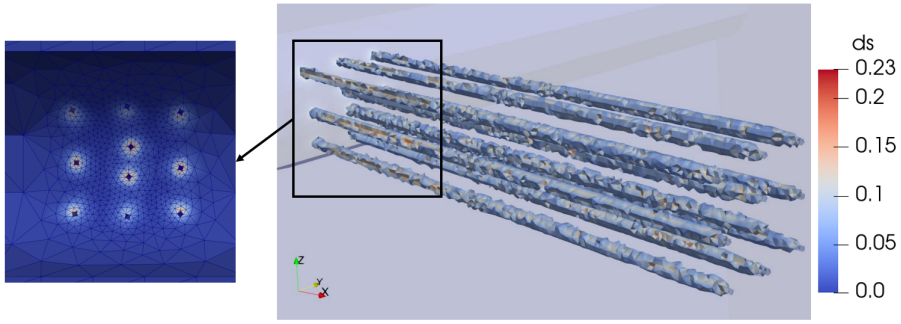

Figure 7: Distribution of the shear damage according to the excavation of heater boreholes

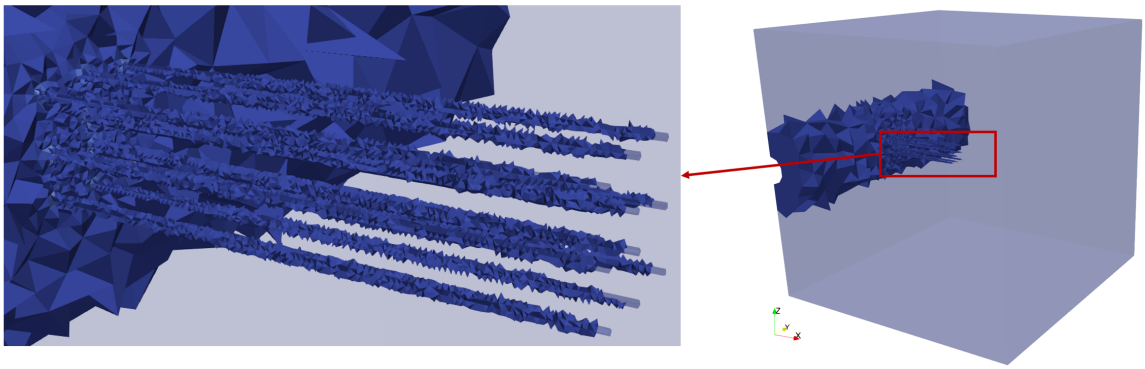

Figure 8: Distribution of the elements with greater than 10 times value higher than initial permeability k_0

By incorporating the seepage phenomenon, the numerical simulation results for pore pressure is depicted in Figure 9. The pore pressure has a reduction because of the borehole excavation at the beginning of the simulation. After the holding phase, the first heating phase begins at 273^{rd} day. The simulation results closely align with the experimental findings for both the heating and cooling phases, with one exception. The data from sensors 01 and 05, which are situated far from the heating section, exhibit some disparities. Regarding the reduction observed in the measured data from sensor 05 of CRQ1720 before the end of the first heating phase, it is likely attributable to a technical issue during the experiment. As for the 01 sensors, located at the deepest region approximately 5 meters below the end

of the boreholes, the measured pore pressure shows minimal impact from the two heating phases. This discrepancy, particularly evident in the sensors of CRQ1720, could indicate the presence of an initial fracture zone between the BDZ and sensor 01 of CRQ1720.

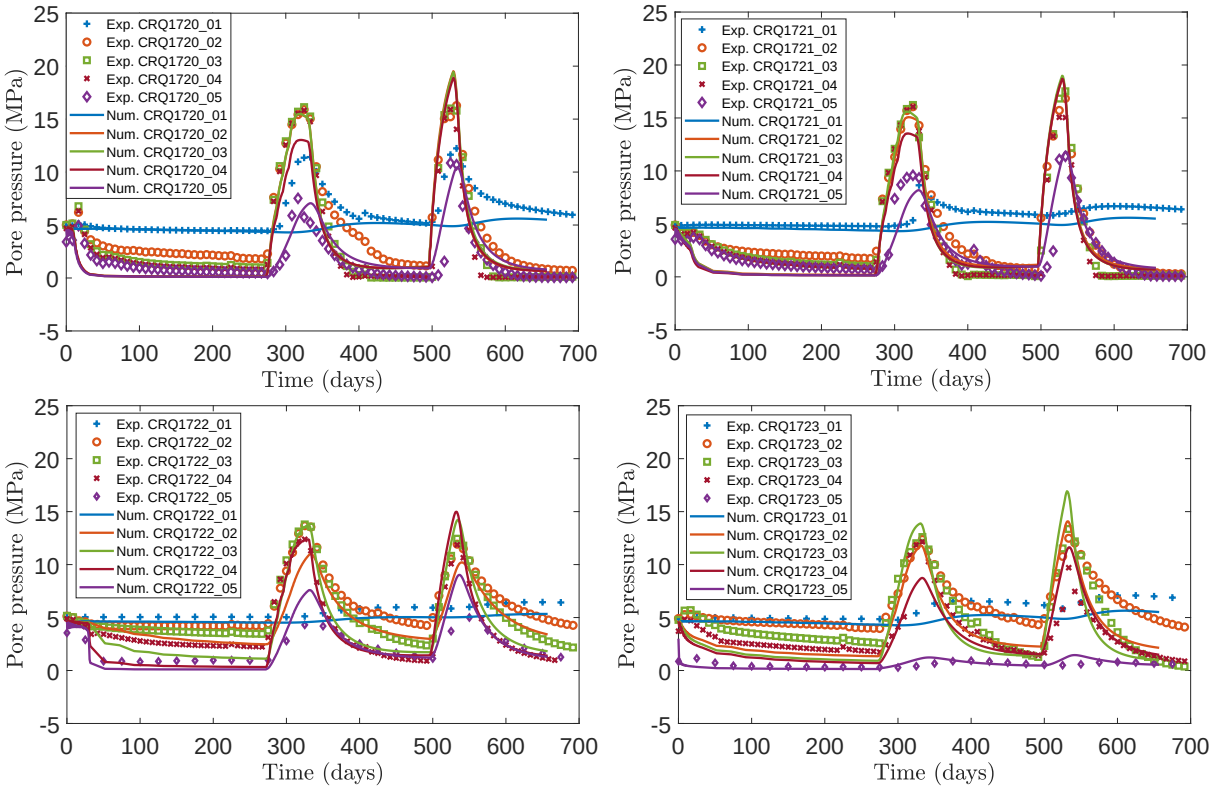

Figure 9: Evolution of pore pressure at the sensor points of CRQ 1720-1723, comparing the experimental results and numerical results

Of note, sensors 03 of four boreholes are located in the mid-plane of the heating area, which is considered the most important region to study failure behavior. As such, the evolution of pore pressure at the sensor 03 locations is presented together in Figure 10. The location of four sensor 03 are presented in the right figure with different colored icons. Among them, the sensors CRQ1720 and 1721 are located inside the square surrounded by ten heaters, while CRQ1722 and 1723 are located outside of it. It results in the blue and orange dotted curves of the pore pressure having higher peak values than the green and red ones. (The colors of the curves and icons are the same.) This feature is well reproduced in the numerical results. However, the simulation results have the limitation. Some features,

such as: i) the green dotted curve being slightly higher than the red one; ii) the green and red dotted curves having a slower reduction than the blue and orange ones during the two cooling phases, are not able to be reproduced in the simulation. The model used in this work has its limitation. To improve the simulation and address these issues, considering the elasto-plastic behavior of the material and incorporating an open-close crack function in the numerical model could be beneficial. However, the reason about these differences between experimental and numerical results may be complex. The evolution of pore pressure in the in-situ test can indeed be influenced by various factors, including the leakage of resin or the presence of initial fractures in the rock. These factors can introduce complexities and uncertainties in the behavior of pore pressure.

To gain a deeper understanding of the damage effects observed during the in-situ heating test, we present an additional set of numerical results depicted in Figure 11. These results are obtained through a thermo-poro-elastic model simulation that does not take into account the influence of damage. Similar to Figure 10, the numerical results of pore pressure is compared with the experiment data of the sensors 03. While the trends of the curves are effectively reproduced, the peak value in the numerical results is notably higher than that observed in the experimental data. This discrepancy can be attributed to the absence of the BDZ, where pore water is trapped due to the low permeability of COx claystone. Consequently, the pore pressure in the numerical simulation increases to an unrealistic value during the heating phases.

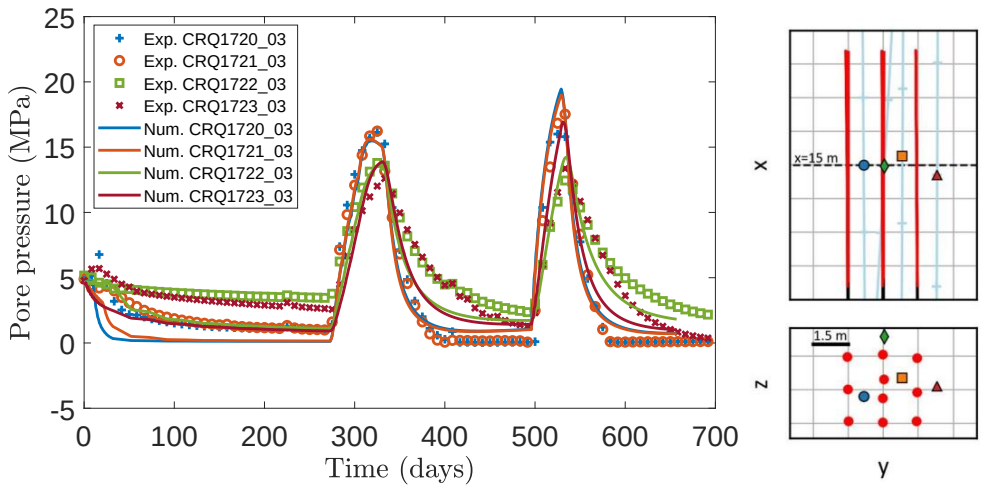

Figure 10: Evolution of pore pressure at the sensor points of sensor 03, comparing the experimental results and numerical results with considering damage effect

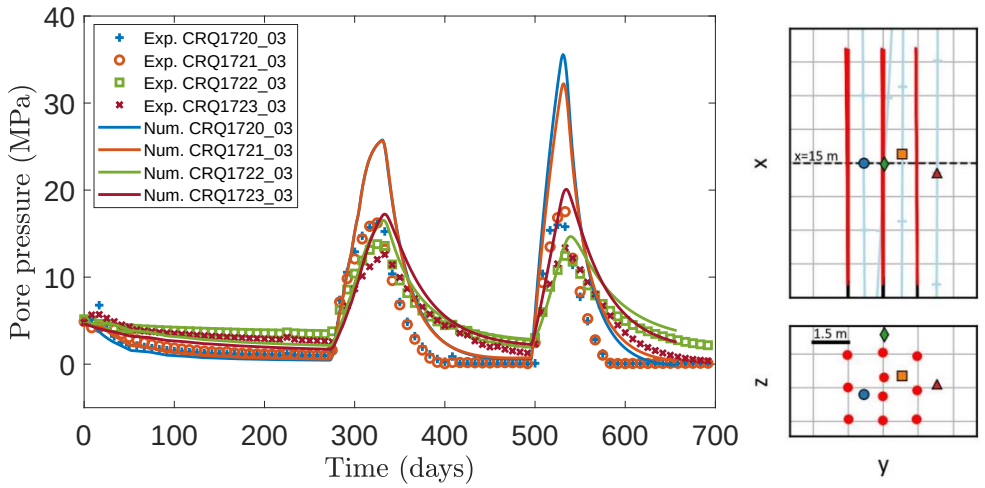

Figure 11: Evolution of pore pressure at the sensor points of sensor 03, comparing the experimental results and numerical results without considering damage effect

Furthermore, Figure 12 displays the distribution of pore pressure at the two ends of the heating phase, taking into account the damage effect. In contrast, Figure 13 represents the distribution of pore pressure in a simulation where the damage effect is not considered, allowing for a meaningful comparison between the two scenarios. Similar to the temperature results, the pore pressure induced by the second heating phase is higher compared to the pore pressure induced by the first heating phase. Additionally, due to the failure of the

heater, the overpressure zone that was previously observed around the three top boreholes is no longer present. In Figure 12, it is evident that the presence of the BDZ results in a reduction of pore pressure around the boreholes. On the other hand, unlike the overpressure zone is more concentrated in the case without damage consideration, the presence of the BDZ leads to a larger and more uniform overpressure zone. As a consequence, the distribution of pore pressure, which is influenced by the presence of the BDZ, can directly impact the formation of thermal damage.

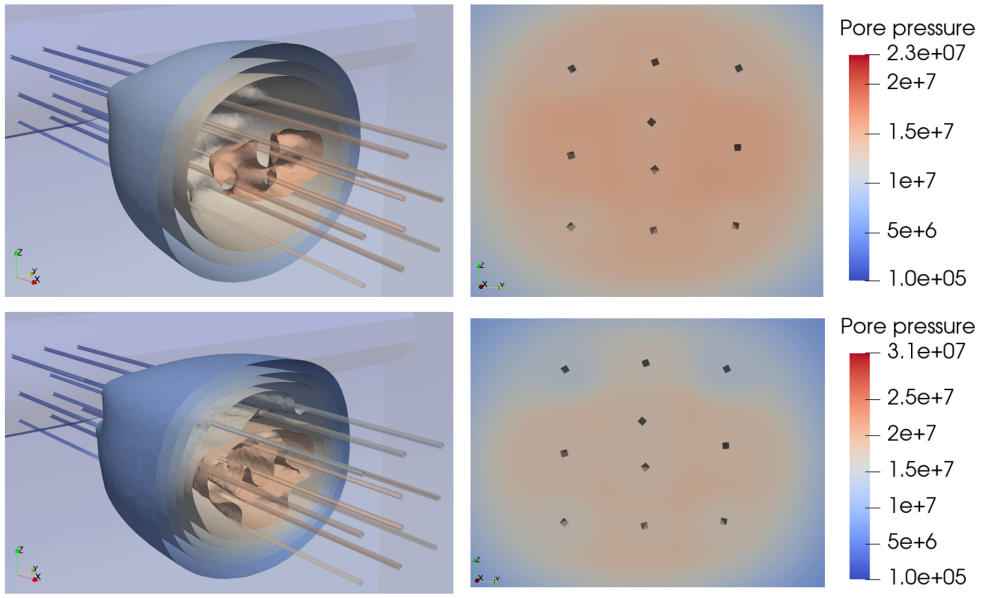

Figure 12: Distribution of pore pressure (Pa) at the end of the first heating phase (top) and the end of second heating phase (bottom), simulation with considering damage effect

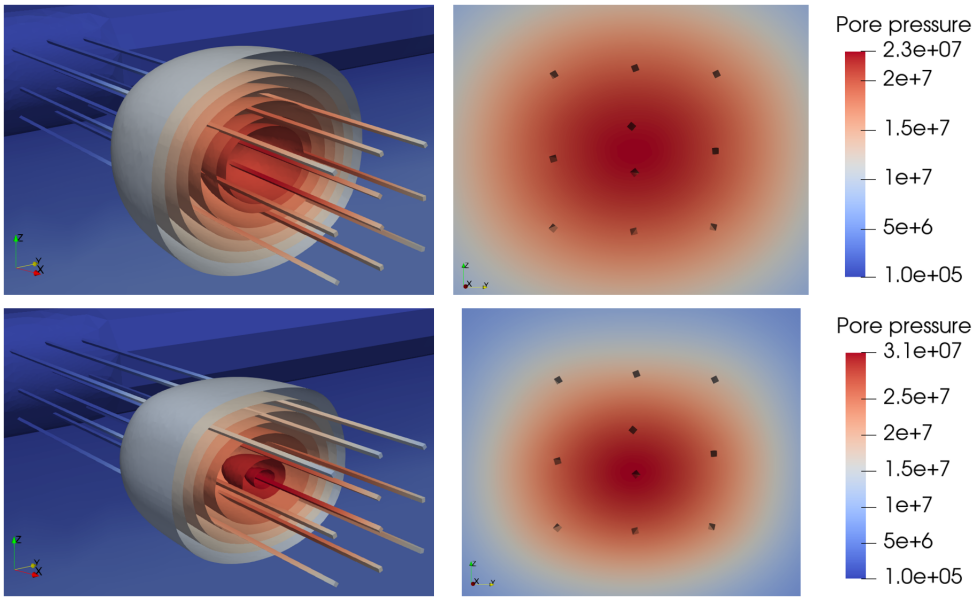

Figure 13: Distribution of pore pressure (Pa) at the end of the first heating phase (top) and the end of second heating phase (bottom), simulation without considering damage effect

After successfully reproducing the variation of pore pressure, the thermal damage evolution is now investigated. It is noticed that it is very difficult to quantitatively measure intensity of thermal damage in in-situ experiment. Only distributions of micro-cracks are characterized through drilled samples. Therefore, the comparison between modeling and experiment is mainly focused on the extent of cracked or damaged zone. Figure 14 shows the distribution of tensile damage due to the two heating phases. The distribution of shear damage is not shown here, since the shear damage is almost not changed during the heating. The maximum value of tensile damage indicates that there is almost no hydro-thermal damage at the end of the first heating. A few damage appears due to the second heating, but no macro crack is predicted to see. The damaged zone is mainly located around the lower hole of the two center boreholes, because the highest pore pressure can be found in this area.

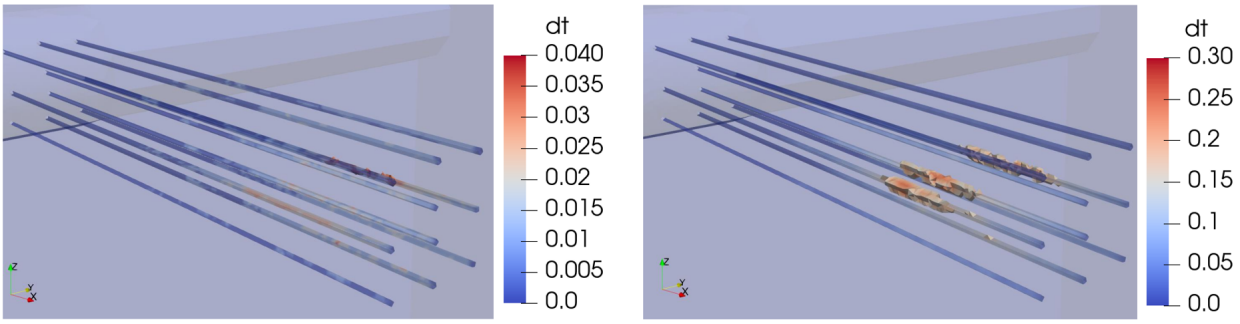

Figure 14: Distribution of the tensile damage according to the first heating phase (left) and second heating phase (right)

In this subsection, a simulation of the CRQ test is conducted by incorporating the consideration of damage. Both excavation-induced damage and heating-induced damage are reproduced using the proposed double phase field method. In addition, the effect of the BDZ on reducing the pore pressure in the over-pressure zone around the boreholes is taken into account. After successfully reproducing the peak value of the pore pressure, the simulation results can be used to predict the hydro-thermal fracture that occurs at the end of the simulation. Overall, this approach provides a convincing and effective result for predicting and studying the thermo-hydromechanical behavior of claystone in the context of the CRQ test.

5.3.1. Study of material heterogeneity

As introduced before, given that material heterogeneity plays an important role during the cracking process of COx claystone, it should be considered in the simulation of CRQ test. According to the previous studies [51, 43], both the solid clay matrix and COx claystone are assumed to exhibit transversely isotropic elastic behavior, while the equivalent inclusion is assumed to be isotropic. The parameters used in this work for homogenization and random distribution are presented in detail in Table 4 based on the previous studies [52, 43]. It is worth noting that the elastic properties of constituent phase are identified by using an inverse optimization procedure by using the Equations (28) and (29). After taking typical values for calcite and quartz inclusions, the elastic parameters of clay matrix are calculated

from the measured macroscopic values for a given set of porosity and mineral composition. With these values, the homogenized elastic properties can be obtained: $E_{\parallel}^{hom} = 6.08$ GPa, $E_{\perp}^{hom} = 4.42$ GPa, $\nu_{\parallel}^{hom} = 0.28$, $\nu_{\parallel\perp}^{hom} = 0.33$ and $G_{\parallel\perp}^{hom} = 2.7$ GPa. These macroscopic elastic properties are suitable compare with the measured parameters of COx claystone from [51].

Based on previous simulation results that considered a uniform rock, it was observed that the critical failure behavior occurred in the vicinity of the heated part of boreholes. Consequently, we have limited our study of material heterogeneity to the area with a refined mesh, as illustrated in Figure 3. In this way, Figure 15 illustrates a representative example of the random distribution of porosity and volumetric fraction of inclusions. Since the Weibull distribution function is widely used in many situations, it is also adopted here. The involved parameters are chosen so that the variation of porosity and inclusion fraction correspond to typical variability of these parameters observed on COx claystone.

Table 4: Parameter of material heterogeneity for CRQ simulation

Parameters	Value
Young's modulus (solid matrix)	$E_{\parallel}^{m} = 3.6$ GPa, $E_{\perp}^{m} = 2.4$ GPa
Poisson's ratio (solid matrix)	$\nu_{\parallel}^{m} = 0.3$, $\nu_{\parallel\perp}^{m} = 0.3$
Shear modulus (solid matrix)	$G_{\parallel\perp}^{m} = 1.02$ GPa
Young's modulus (inclusion)	$E_i = 98$ GPa
Poisson's ratio (inclusion)	$\nu_i = 0.15$
Inclusion volume fraction	$\beta_i = 0.4$
Pore volume fraction	$\beta_p = 0.16$
Homogeneity index	$m_i = m_p = 1.5$

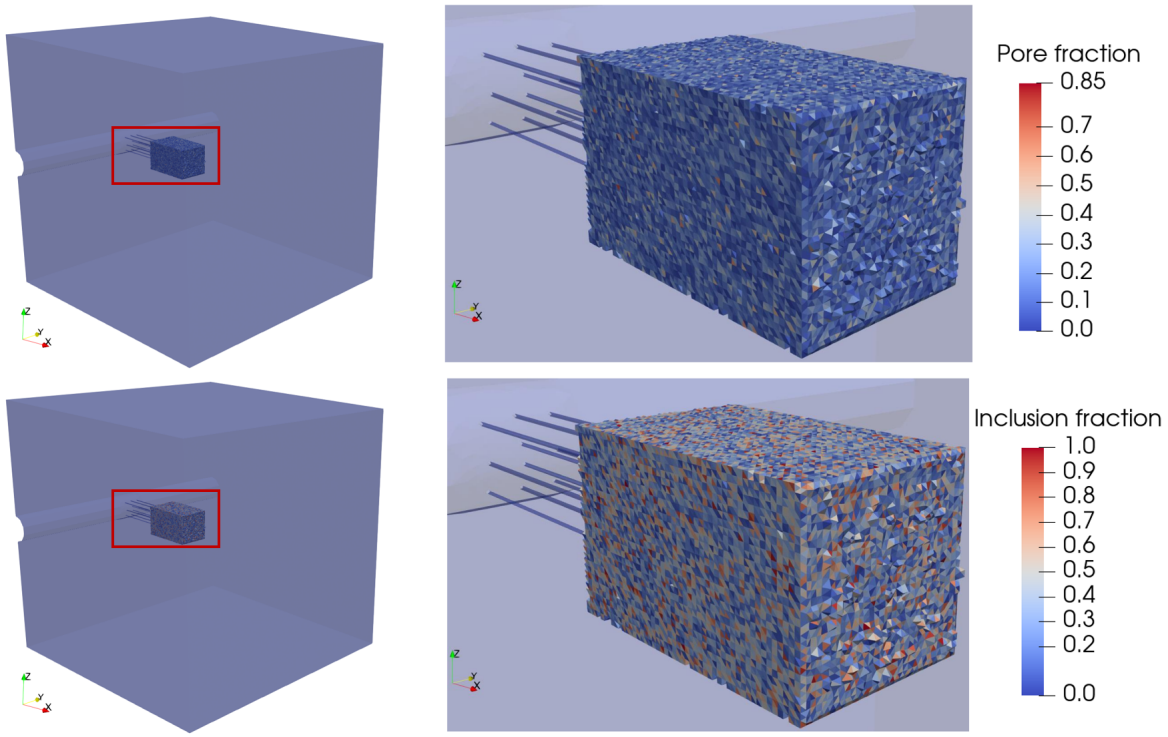

Figure 15: Distribution of pores volume fraction (top) and inclusion volume fraction (bottom)

Since we anticipate that the simulation outcomes will vary depending on the random distribution of pores and inclusions, we selected three simulations (denotes Num. 1, 2 and 3) with different sets of random distribution for analysis. At first, Figure 16 shows the distribution of shear damage induced to excavation by using three different sets of random distribution. The maximum value of d^s differs among the three simulations due to variations in the homogenized elastic properties resulting from differences in porosity and inclusion volume fraction. However, the form of BDZ remains unchanged compared to the simulation results considering a uniform rock. Similarly, this BDZ leads to the mentioned seepage phenomenon, which can reduce the pore pressure at the study points as shown in Figure 17. Even though the three simulations used different random distributions, the resulting numerical results are identical as depicted in Figure (a-c). For instance, the three curves of CRQ1720-03 are exactly coincided as shown in Figure (d).

Additionally, upon comparing the numerical results to the previous subsection, it is evident that the values are reduced, particularly during the cooling phases and at the end

of the second heating phase. To investigate this difference, a comparison of the distribution between the two simulations is provided in Figure 18. At the initial stage, the distribution of pore pressure does not show any non-uniform characteristics. Material heterogeneity is only taken into account for the stiffness matrix in the mechanical field, while major parameters in the pore pressure field, such as permeability, are not considered. In other words, the mechanical heterogeneity is not strong enough to significantly influence the pore pressure field.

However, the principal difference between the two simulation results lies in the pore pressure within the BDZ. Comparing the simulation with considering heterogeneity to the one without, there is a slightly greater reduction in pore pressure within the BDZ in the simulation that considers heterogeneity. This significant reduction improves the evolution of pore pressure during the cooling phases, bringing it closer to the experimental data. The reason for this reduction in the BDZ can be attributed to the presence of a larger BDZ due to the weak regions obtained through the random distribution of pores.

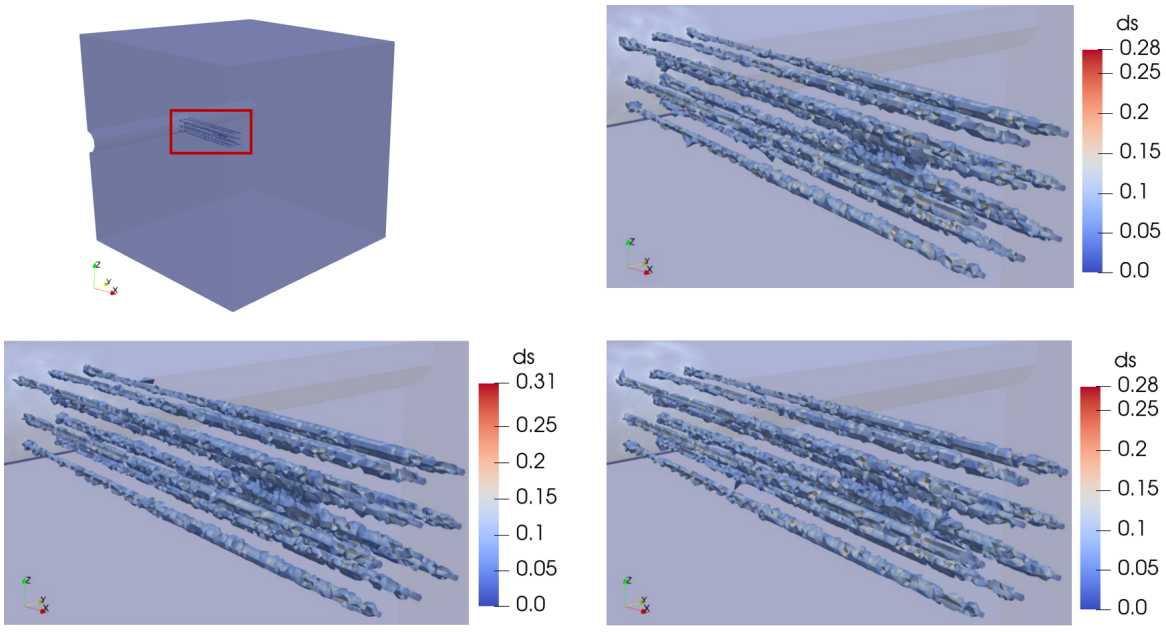

Figure 16: Distribution of shear damage induced by excavation, simulated by using different random distribution of pore and inclusion: Num. 1, 2 and 3

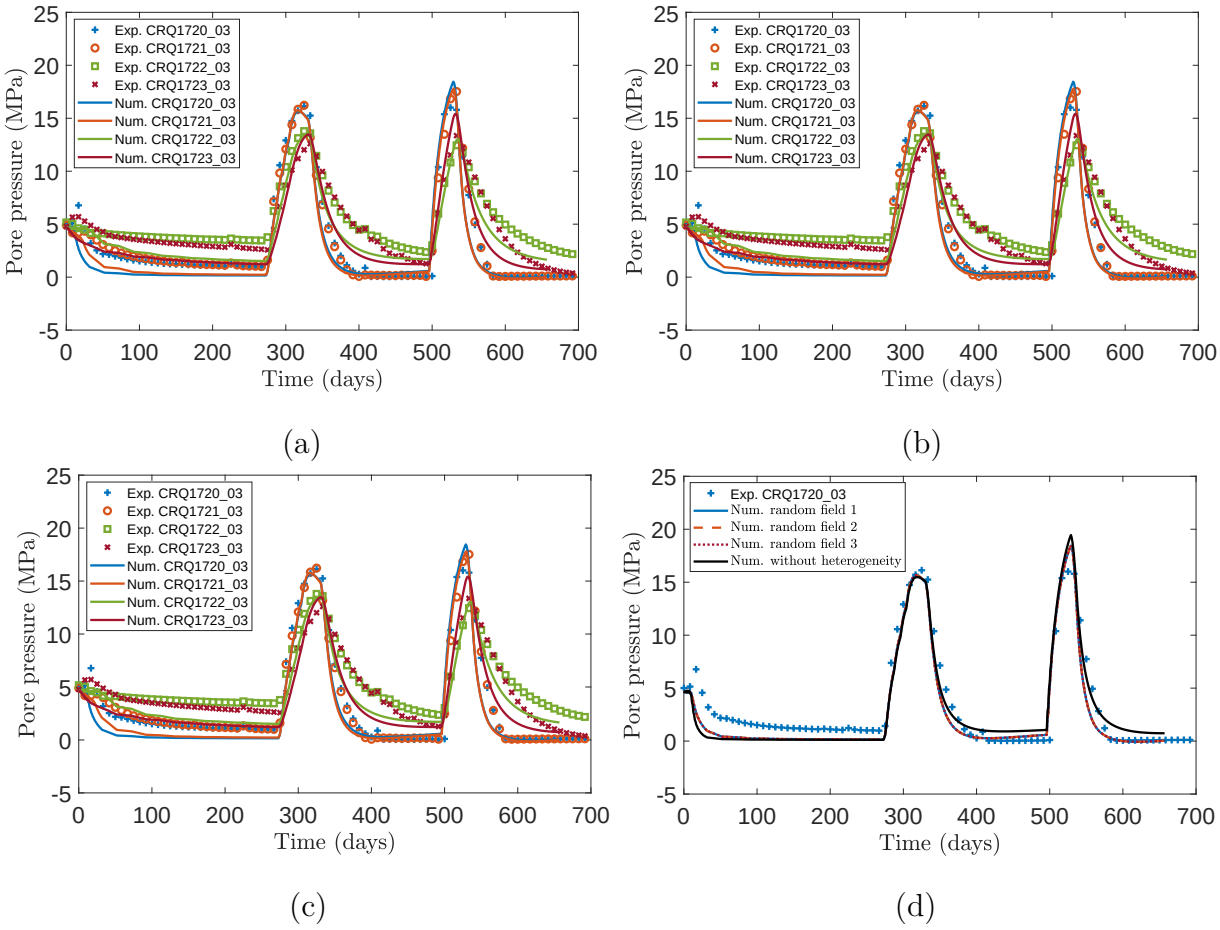

Figure 17: Evolution of pore pressure at sensor 03 of CRQ 1720-1723 for simulations using different distributions of pores and inclusions: Num. 1, 2 and 3 (a-c), and comparison of pore pressure evolution at sensor CRQ 1720-03 for simulations using different distributions of pores and inclusions: Num. 1, 2 and 3, as well as the simulation result without considering heterogeneity (d)

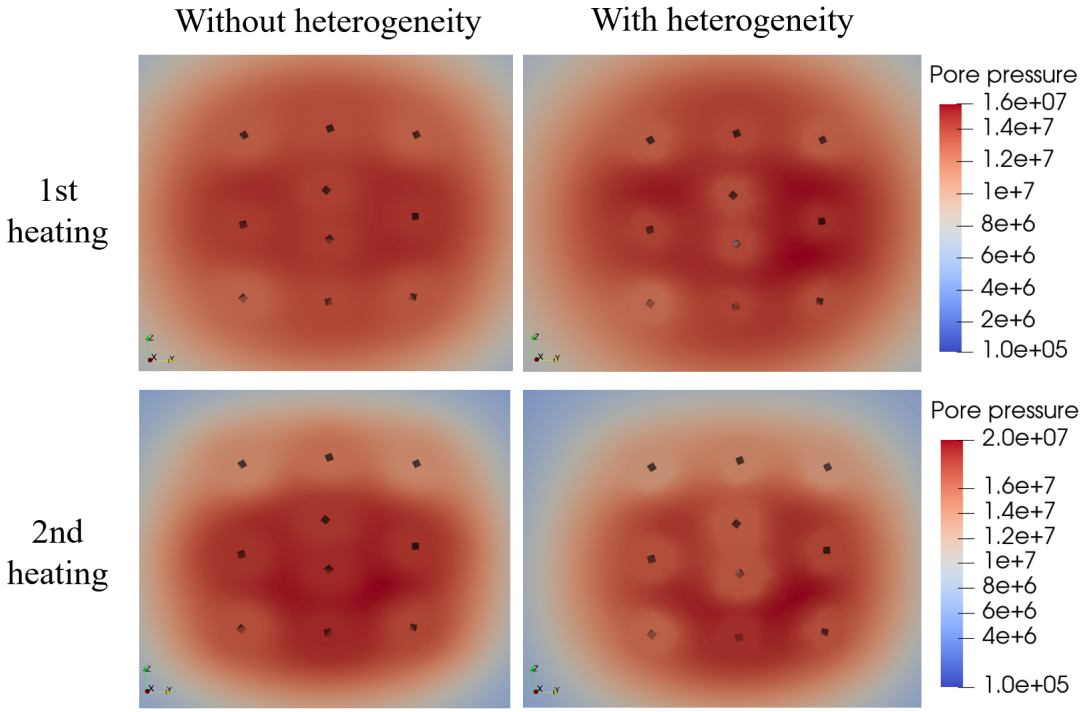

Figure 18: Distribution of pore pressure (Pa) at the end of the first and second heating: comparison between the simulation with and without considering damage effect

Figure 19 shows the distribution of tensile damage at the end of the second heating phase. It is worth noting that the tensile damage induced by the first heating phase is not shown since the maximum value of d^t is less than 0.1. It is reasonable to observe that the maximum values of d^t, which are 0.43, 0.79, and 0.83, respectively, are greater compared to the uniform simulation ($d^t = 0.3$) due to the presence of a weak region. The element with this maximum value is located between the two central boreholes as expected. Since there are no elements with high damage variables outside of this area in all three simulations, it appears that the results are consistent.

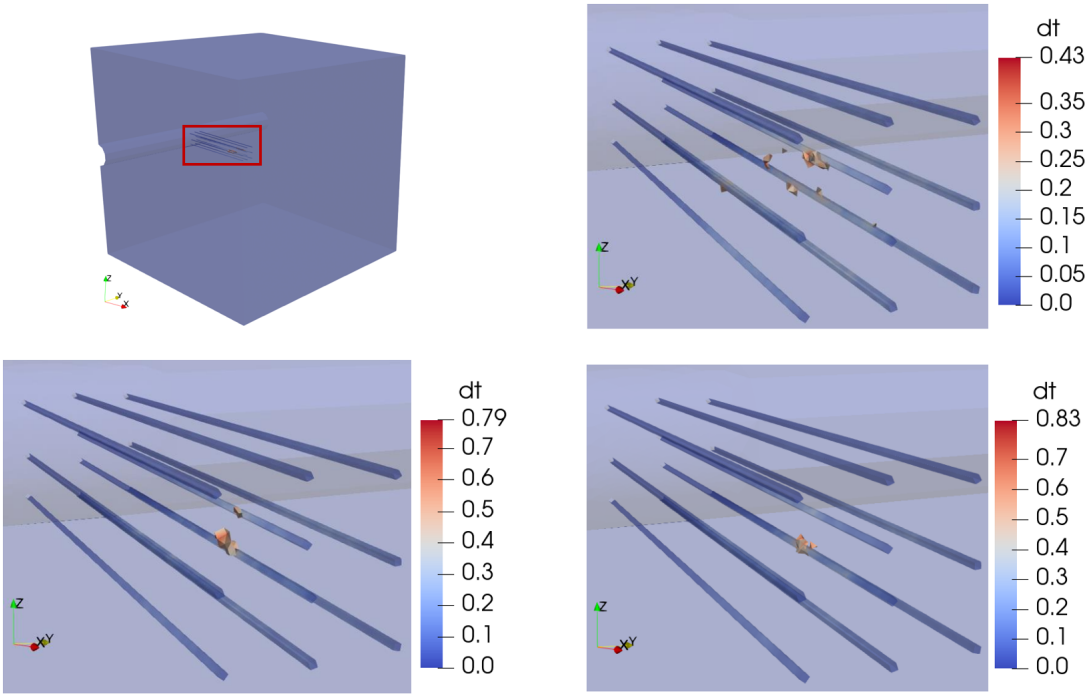

Figure 19: Distribution of tensile damage at end of second heating phase, simulated by using random distribution of pore and inclusion: Num. 1, 2 and 3

By considering the material heterogeneity, a more realistic representation of the rock behavior is achieved, and the simulation better captures the behavior of pore pressure in the BDZ, resulting in improved agreement with experimental data during the cooling phases. Additionally, the presence of weak regions in the rock, such as pores and inclusions, can influence the occurrence of thermal fractures.

However, it should be noted that the simulation considering material heterogeneity ensures that the overall features of the thermal crack remain unchanged compared to the simulation without considering heterogeneity. Specifically, the thermal damage mainly appears between the two center boreholes, and a macroscopic crack does not form (damage variable d^t or $d^s = 1$).

6. Conclusion

This study proposes a THM modeling approach that incorporates the phase-field method to account for damage effects. The model is capable of identifying both tensile and shear

cracks induced by THM coupling behavior. To test the model's effectiveness, it is applied to simulate the CRQ test. The results show that the model accurately reproduces the evolution of temperature and pore pressure at sensor points and the corresponding damage zone. The study also finds that the THM coupling process is significantly affected by the BDZ induced seepage phenomenon. The excavation and heating induced damage zone are identified as shear and tensile damage, respectively. Moreover, the study verifies the model's consistency with material heterogeneity. It is worth noticing that in the present study, the mechanical properties are identified from typical laboratory tests such as triaxial compression tests. The parameters related to fluid flow and heat diffusion are chosen by Andra, for all the teams involved in the DECOVALEX project. There is no fitting of parameters with respect to the in-situ experiment. Therefore, the numerical simulation presented here represents an interesting phase of validation of the proposed numerical model. However, further simulations of other experiments are still useful for a deep validation of the proposed model. Moreover, other important features, such as the variation of critical fracture energy with temperature change, should also be investigated.

Acknowledgment:

This work is jointly supported by the French National Agency for radioactive waste management (ANDRA), the DECOVALEX project and the National Natural Science Foundation of China (No. 12202099). DECOVALEX is an international research project comprising participants from industry, government and academia, focusing on development of understanding, models and codes in complex coupled problems in sub-surface geological and engineering applications. The authors appreciate and thank the DECOVALEX-2023 Funding Organizations for their financial and technical support of the work described in this paper. The statements made in the paper are, however, solely those of the authors and do not necessarily reflect those of the Funding Organizations.

Appendix: Positions of sensors and dates of the heater boreholes drilling

In order to identify the coordinates of the sensor points, the origin (0,0,0) of the model domain is located at the mid-distance between the heads of borehole CRQ1720 and CRQ1721. In this way, the studied 3D domain of cube with a side length of 50 m vary between x=-2.6 m to 47.4 m (parallel to the heater boreholes); y=-25.0 m to 25.0 m (parallel to the GCS gallery) and z=-25 m to 25 m (perpendicular to the heater boreholes and the GCS gallery). In this defined coordinate system, the position of sensor points are shown as follows:

Table 5: The position of sensor points used in simulation of CRQ test

Sensor	Coordinate-x (m)	Coordinate-y (m)	Coordinate-z (m)
CRQ1720-01	24.99	0.91	-0.21
CRQ1720-02	17.99	0.86	-0.27
CRQ1720-03	15.00	0.84	-0.29
CRQ1720-04	12.00	0.82	-0.31
CRQ1720-05	8.00	0.79	-0.32
CRQ1721-01	25.39	-0.86	0.65
CRQ1721-02	18.38	-0.84	0.55
CRQ1721-03	15.38	-0.82	0.51
CRQ1721-04	12.38	-0.81	0.47
CRQ1721-05	8.38	-0.79	0.43
CRQ1722-01	24.92	-0.57	3.73
CRQ1722-02	17.90	-0.21	2.75
CRQ1722-03	14.93	-0.05	2.34
CRQ1722-04	11.97	0.10	1.94
CRQ1722-05	8.01	0.32	1.41
CRQ1723-01	24.57	-2.34	0.27
CRQ1723-02	19.56	-2.33	0.21
CRQ1723-03	14.56	-2.31	0.15
CRQ1723-04	9.57	-2.29	0.1
CRQ1723-05	4.57	-2.27	0.07

533 The detail date of the main operations during CRQ test is:

534 • The drift of GCS gallery: 15^{th} September 2010

535 • The drift of heater boreholes: between 20^{th} and 30^{30} October 2017 (see Table)

536 • The first heating phase: between 3^{rd} June and 31^{st} July 2019

- The second heating phase: between 13^{th} January and 14^{th} February 2020

Table 6: Dates of the heater boreholes drilling for CRQ test

Borehole	Drilling date	Borehole	Drilling date
CRQ1701	14/09/2018	CRQ1706	03/09/2018
CRQ1702	13/09/2018	CRQ1707	05/09/2018
CRQ1703	27/09/2018	CRQ1708	07/09/2018
CRQ1704	02/10/2018	CRQ1709	11/09/2018
CRQ1705	04/10/2018	CRQ1710	24/09/2018

References

[1] G. Armand, F. Leveau, C. Nussbaum, R. deLaVaissiere, A. Noiret, D. Jaeggi, P. Landrein, C. Righini, Geometry and properties of the excavation induced fractures at the meuse-haute-marne url drifts., Rock Mech. Rock Eng. 47 (2014) 21–41.

[2] D. Seyedi, a. at, Upscaling thm modelling from small-scale to full-scale in-situ experiment in the callovo-oxfordian claystone., Int. J. of Rock Mechanics and Mining Sciences 144 (104582) (2021) 1365–1609.

[3] N. Conil, V. Manon, C. Plua, V. M. N., D. Seyedi, G. Armand, In situ investigation of the thm behavior of the callovo-oxfordian claystone., Rock Mechanics and Rock Engineering online (2020).

[4] C.-F. Tsang, O. Stephansson, L. Jing, F. Kautsky, Decovalex project: from 1992 to 2007, Environmental Geology 57 (6) (2009) 1221–1237.

[5] J. T. Birkholzer, A. E. Bond, J. A. Hudson, L. Jing, C.-F. Tsang, H. Shao, O. Kolditz, Decovalex-2015: an international collaboration for advancing the understanding and modeling of coupled thermo-hydro-mechanical-chemical (thmc) processes in geological systems (2018).

[6] J. T. Birkholzer, C.-F. Tsang, A. E. Bond, J. A. Hudson, L. Jing, O. Stephansson, 25 years of decovalex-scientific advances and lessons learned from an international research collaboration in coupled subsurface processes, International Journal of Rock Mechanics and Mining Sciences 122 (2019) 103995.

[7] J. Oliver, Modelling strong discontinuities in solid mechanics via strain softening constitutive equations, part 1: fundamentales, Internat. J. Numer. Methods Engrg. 39 (1996) 3575–3600.

[8] N. Moes, J. Dolbow, T. Belytschko, A finite element method for crack growth without remeshing, Internat. J. Numer. Methods Engrg. 46 (1999) 131–150.

[9] N. Moes, C. Stolz, N. Chevaugeon, P. E. Bernard, A level set based model for damage growth: The thick level set approach, International Journal for Numerical Methods in Engineering 86 (2010) 358–380.

[10] P. E. Bernard, N. Moes, N. Chevaugeon, Damage growth modeling using the thick level set (tls) approach: Efficient discretization for quasi-static loadings, Computer Methods in Applied Mechanics and Engineering 233-236 (2012) 11–27.

[11] G. A. Francfort, J.-J. Marigo, Revisiting brittle fracture as an energy minimization problem, Journal of the Mechanics and Physics of Solids 46 (8) (1998) 1319–1342.

[12] B. Bourdin, G. A. Francfort, J.-J. Marigo, Numerical experiments in revisited brittle fracture, Journal of the Mechanics and Physics of Solids 48 (4) (2000) 797–826.

[13] C. Miehe, M. Hofacker, F. Welschinger, A phase field model for rate-independent crack propagation: Robust algorithmic implementation based on operator splits, Computer Methods in Applied Mechanics and Engineering 199 (45-48) (2010) 2765–2778.

[14] M. J. Borden, C. V. Verhoosel, M. A. Scott, T. J. Hughes, C. M. Landis, A phase-field description of dynamic brittle fracture, Computer Methods in Applied Mechanics and Engineering 217 (2012) 77–95.

[15] C. Miehe, M. Hofacker, L.-M. Schänzel, F. Aldakheel, Phase field modeling of fracture in multi-physics problems. part ii. coupled brittle-to-ductile failure criteria and crack propagation in thermo-elastic–plastic solids, Computer Methods in Applied Mechanics and Engineering 294 (2015) 486–522.

[16] J. Choo, W. Sun, Coupled phase-field and plasticity modeling of geological materials: From brittle fracture to ductile flow, Computer Methods in Applied Mechanics and Engineering 330 (2018) 1–32.

[17] J. Fang, C. Wu, J. Li, Q. Liu, C. Wu, G. Sun, L. Qing, Phase field fracture in elasto-plastic solids: variational formulation for multi-surface plasticity and effects of plastic yield surfaces and hardening, International Journal of Mechanical Sciences (2019).

[18] X. Zhang, S. W. Sloan, C. Vignes, D. Sheng, A modification of the phase-field model for mixed mode crack propagation in rock-like materials, Computer Methods in Applied Mechanics and Engineering 322 (2017) 123–136.

[19] E. C. Bryant, W. Sun, A mixed-mode phase field fracture model in anisotropic rocks with consistent kinematics, Computer Methods in Applied Mechanics and Engineering 342 (2018) 561–584.

[20] B. Evans, J. T. Fredrich, T.-F. Wong, The brittle-ductile transition in rocks: Recent experimental and theoretical progress, The Brittle-Ductile Transition in Rocks, Geophys. Monogr. Ser 56 (1990) 1–20.

[21] T.-f. Wong, P. Baud, The brittle-ductile transition in porous rock: A review, Journal of Structural Geology 44 (2012) 25–53.

[22] F. Fei, J. Choo, A phase-field method for modeling cracks with frictional contact, International Journal for Numerical Methods in Engineering 121 (4) (2020) 740–762.

[23] F. Fei, J. Choo, A phase-field model of frictional shear fracture in geologic materials, Computer Methods in Applied Mechanics and Engineering 369 (2020) 113265.

[24] J. Ulloa, J. Wambacq, R. Alessi, E. Samaniego, G. Degrande, S. François, A micromechanics-

based variational phase-field model for fracture in geomaterials with brittle-tensile and compressive-ductile behavior, Journal of the Mechanics and Physics of Solids 159 (2022) 104684.

[25] T. You, H. Waisman, Q.-Z. Zhu, Brittle-ductile failure transition in geomaterials modeled by a modified phase-field method with a varying damage-driving energy coefficient, International Journal of Plasticity 136 (2021) 102836.

[26] Z. Yu, J. F. Shao, M. N. Vu, G. Armand, Numerical study of thermo-hydro-mechanical responses of in situ heating test with phase-field model., International Journal of Rock Mechanics and Mining Sciences 138 (2021) 104542.

[27] F. Fei, J. Choo, Double-phase-field formulation for mixed-mode fracture in rocks, Computer Methods in Applied Mechanics and Engineering 376 (2021) 113655.

[28] Z. Yu, Y. Sun, M. N. Vu, J. F. Shao, Modeling of mixed cracks in rock-like brittle materials under compressive stresses by a double-phase-field method, Rock Mechanics and Rock Engineering online (2023).

[29] C. Miehe, F. Welschinger, M. Hofacker, Thermodynamically consistent phase-field models of fracture: variational principles and multi-field fe implementations, International Journal for Numerical Methods in Engineering 83 (10) (2010) 1273–1311.

[30] J.-Y. Wu, A unified phase-field theory for the mechanics of damage and quasi-brittle failure, Journal of the Mechanics and Physics of Solids 103 (2017) 72–99.

[31] O. Coussy, Poromechanics, John Wiley & Sons, 2004.

[32] A. H.-D. Cheng, Poroelasticity, Vol. 27, Springer, 2016.

[33] V. Lubarda, D. Krajcinovic, S. Mastilovic, Damage model for brittle elastic solids with unequal tensile and compressive strengths, Engineering Fracture Mechanics 49 (5) (1994) 681–697.

[34] S. Murakami, Continuum damage mechanics: a continuum mechanics approach to the analysis of damage and fracture, Vol. 185, Springer Science & Business Media, 2012.

[35] Z. Yu, J. Shao, G. Duveau, M.-N. Vu, G. Armand, Numerical modeling of deformation and damage around underground excavation by phase-field method with hydromechanical coupling, Computers and Geotechnics 138 (2021) 104369.

[36] P. DeBuhan, L. Dormieux, On the validity of the effective stress concept for assessing the strength of saturated porous materials: a homogenization approach, J. Mech. Phys. Solids 44 (1996) 1649–1677.

[37] D. Lydzba, J. F. Shao, Stress equivalence principle for saturated porous media, Comptes Rendus Mecanique 330 (2002) 297–303.

[38] J. Kim, H. Tchelepi, R. Juanes, Stability and convergence of sequential methods for coupled flow and geomechanics: Fixed-stress and fixed-strain splits, Computer Methods in Applied Mechanics and Engineering 200 (2011) 1591–1606.

[39] B. Bourdin, G. A. Francfort, J.-J. Marigo, The variational approach to fracture, Journal of elasticity 91 (1-3) (2008) 5–148.

[40] J. C. Robinet, P. Sardini, D. Coelho, J. C. Parneix, D. Pret, S. Sammartino, E. Boller, S. Altmann, Effects of mineral distribution at mesoscopic scale on solute diffusion in a clay-rich rock: Example of the callovo-oxfordian mudstone (bure, france), Water resources research 48 (2012) W05554.

[41] T. Mori, K. Tanaka, Averages stress in matrix and average elastic energy of materials with misfitting inclusions, Acta Metall. 21 (1973) 571–574.

[42] A. Giraud, Q. Huynh, D. Hoxha, D. Kondo, Application of results on eshelby tensor to the determination of effective poroelastic properties of anisotropic rocks-like composites, International Journal of Solids and Structures 44 (11) (2007) 3756–3772.

[43] J. J. Zhao, W. Q. Shen, Z. B. Shao, J F anc Liu, M. N. Vu, A constitutive model for anisotropic clay-rich rocks considering micro-structural composition, International Journal of Rock Mechanics and Mining Sciences 151 (2022) 105029.

[44] D. Seyedi, G. Armand, N. Conil, M. Vitel, M. N. Vu, On the thermo-hydro-mechanical pressurization in callovo-oxfordian claystone under thermal loading., Poromechanics VI 2017 (2017) 754–761.

[45] D. M. Seyedi, G. Armand, A. Noiret, "transverse action"–a model benchmark exercise for numerical analysis of the callovo-oxfordian claystone hydromechanical response to excavation operations, Computers and Geotechnics 85 (2017) 287–305.

[46] G. Armand, F. Bumbieler, N. Conil, R. delaVaissiere, J. M. Bosgiraud, M. N. Vu, Main outcomes from in situ thermo-hydro-mechanical experiments programme to demonstrate feasibility of radioactive high-level waste disposal in the callovo-oxfordian claystone., J. of Rock Mechanics and Geotechnical Engineering 9 (2017) 415–427.

[47] P. Braun, Thermo-hydro-mechanical behavior of the callovo-oxfordian claystone: Effects of stress paths and temperature changes, Ph.D. thesis, Université Paris-Est (2019).

[48] Z. Yu, J. Shao, Y. Sun, M. Wang, M. ngoc Vu, C. Plua, Numerical analysis of hydro-thermal fracturing in saturated rocks by considering material anisotropy and micro-structural heterogeneity, International Journal of Rock Mechanics and Mining Sciences 170 (2023) 105457.

[49] J.-Y. Wu, V. P. Nguyen, C. Thanh Nguyen, D. Sutula, S. Bordas, S. Sinaie, Phase field modelling of fracture, Advances in Applied Mechanics 53 (2019) 1–183.

[50] R. de La Vaissiere, G. Armand, J. Talandier, Gas and water flow in an excavation-induced fracture network around an underground drift: A case study for a radioactive waste repository in clay rock., Journal of Hydrology 521 (2015) 141–156.

[51] G. Armand, N. Conil, J. Talandier, D. M. Seyedi, Fundamental aspects of the hydromechanical behaviour of callovo-oxfordian claystone: from experimental studies to model calibration and validation,

662 Computers and Geotechnics 85 (2017) 277–286.
663 [52] F. Farhat, W. Shen, J. Shao, A micro-mechanics based viscoplastic model for clayey rocks, Computers
664 and Geotechnics 89 (2017) 92–102.